

RESEARCH ARTICLE

10.1002/2017JB014339

Key Points:

- We combine time domain thermoreflectance and diamond cell to measure lattice thermal conductivity of Fe-bearing bridgmanite to 120 GPa
- Thermal conductivity of Fe-bearing bridgmanite drops around 45 GPa due to pressure-induced lattice distortion
- Modeling of LLSVP thermal conductivity and CMB heat flux provides insights to thermo-chemical structure and dynamics of lowermost mantle

Supporting Information:

- Supporting Information S1

Correspondence to:

W.-P. Hsieh and J.-F. Lin,
wphsieh@earth.sinica.edu.tw;
afu@jsg.utexas.edu

Citation:

Hsieh, W.-P., F. Deschamps, T. Okuchi, and J.-F. Lin (2017), Reduced lattice thermal conductivity of Fe-bearing bridgmanite in Earth's deep mantle, *J. Geophys. Res. Solid Earth*, 122, 4900–4917, doi:10.1002/2017JB014339.

Received 17 APR 2017

Accepted 16 JUN 2017

Accepted article online 19 JUN 2017

Published online 5 JUL 2017

©2017. American Geophysical Union.
All Rights Reserved.

Reduced lattice thermal conductivity of Fe-bearing bridgmanite in Earth's deep mantle

Wen-Pin Hsieh¹ , Frédéric Deschamps¹ , Takuo Okuchi² , and Jung-Fu Lin³ 

¹Institute of Earth Sciences, Academia Sinica, Taipei, Taiwan, ²Institute for Planetary Materials, Okayama University, Misasa, Japan, ³Department of Geological Sciences, Jackson School of Geosciences, University of Texas at Austin, Austin, Texas, USA

Abstract Complex seismic, thermal, and chemical features have been reported in Earth's lowermost mantle. In particular, possible iron enrichments in the large low shear-wave velocity provinces (LLSVPs) could influence thermal transport properties of the constituting minerals in this region, altering the lower mantle dynamics and heat flux across core-mantle boundary (CMB). Thermal conductivity of bridgmanite is expected to partially control the thermal evolution and dynamics of Earth's lower mantle. Importantly, the pressure-induced lattice distortion and iron spin and valence states in bridgmanite could affect its lattice thermal conductivity, but these effects remain largely unknown. Here we precisely measured the lattice thermal conductivity of Fe-bearing bridgmanite to 120 GPa using optical pump-probe spectroscopy. The conductivity of Fe-bearing bridgmanite increases monotonically with pressure but drops significantly around 45 GPa due to pressure-induced lattice distortion on iron sites. Our findings indicate that lattice thermal conductivity at lowermost mantle conditions is twice smaller than previously thought. The decrease in the thermal conductivity of bridgmanite in mid-lower mantle and below would promote mantle flow against a potential viscosity barrier, facilitating slabs crossing over the 1000 km depth. Modeling of our results applied to LLSVPs shows that variations in iron and bridgmanite fractions induce a significant thermal conductivity decrease, which would enhance internal convective flow. Our CMB heat flux modeling indicates that while heat flux variations are dominated by thermal effects, variations in thermal conductivity also play a significant role. The CMB heat flux map we obtained is substantially different from those assumed so far, which may influence our understanding of the geodynamo.

1. Introduction

In the past decades, seismic observations combined with mineral physics experiments and geodynamic modeling have revealed an Earth's lowermost mantle more complex than previously expected [cf. *Garnero and McNamara*, 2008]. In particular, the large low shear-wave velocity provinces (LLSVPs) observed by seismic tomography may be associated with strong lateral variations in temperature and composition [Trampert *et al.*, 2004; Mosca *et al.*, 2012; Deschamps *et al.*, 2012]. A likely hypothesis for the compositional anomalies in LLSVPs is that they consist of variations in the iron volume fraction by up to a few percent [Trampert *et al.*, 2004; Deschamps *et al.*, 2012]. Furthermore, the phase transition from bridgmanite to post-perovskite [Murakami *et al.*, 2004] may be locally responsible for abrupt changes in shear- and compressional-wave velocities at the bottom of the lower mantle, referred to as the D'' seismic discontinuity [Cobden *et al.*, 2015]. Precise determination of the thermal conductivity, including lattice and radiative components, of the constituting lower mantle materials at relevant conditions would provide critical insight and better constraint on the dynamics of the lowermost mantle and heat flux across core-mantle boundary (CMB) [Lay *et al.*, 2008]. Lateral variations in thermal conductivity triggered by variations in temperature and composition (particularly, iron fraction anomalies) may thus influence the dynamics of LLSVPs, including the generation of thermal plumes at the tops of these provinces, and the amplitude of lateral variations in the CMB heat flux, which have consequences for the geodynamo and the age of the inner core [Buffett, 2000].

Significant efforts have been made to study the lattice and radiative thermal conductivities of the lower mantle materials under extreme conditions, as these two components could play different roles in determining the energy balance and temperature profile in the deep lower mantle. Radiative thermal conductivity of (Fe,Al)-bearing MgSiO₃ bridgmanite at lower mantle conditions has been experimentally measured using optical absorption spectroscopy [Goncharov *et al.*, 2008; Keppler *et al.*, 2008], but the

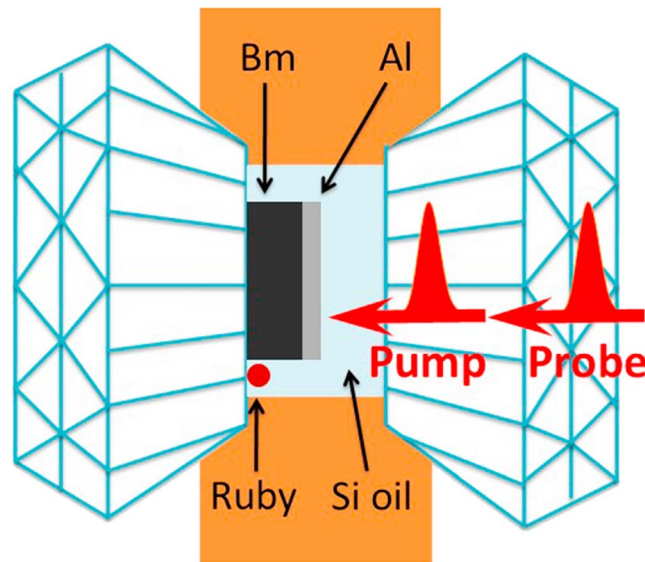


Figure 1. Schematic drawing of the optical pump-probe measurements for the lattice thermal conductivity of bridgmanite (Bm) samples within a diamond anvil cell. An Al film coated on the Bm substrate is a thermal transducer and absorbs thermal energy from optical pump and probe beams. The pressure is measured by ruby fluorescence. Silicone oil serves as the pressure medium.

reported data remain inconclusive with large uncertainties. In contrast, precise measurements of the lattice thermal conductivity of lower mantle materials under extreme pressure-temperature (P - T) conditions are very challenging [Osako and Ito, 1991; Manthilake et al., 2011]. Thus far, very little experimental data are available and its accuracy is insufficient because of the limitations and difficulties of experimental methods. As a result, current estimates of the lattice thermal conductivity of Earth's lower mantle largely rely on theoretical calculations [Hofmeister, 1999; Haigis et al., 2012; Dekura et al., 2013; Ammann et al., 2014; Tang et al., 2014; Stackhouse et al., 2015] or model extrapolations based on results at relatively low P - T conditions, without consideration of the potential effects of chemical composition at the lowermost mantle conditions. Recently, pulsed lasers coupled with high-pressure diamond anvil cell (DAC) have been applied to study the lattice thermal conductivity or diffusivity of deep-Earth materials under extreme conditions [Hsieh et al., 2009; Goncharov et al., 2010, 2015; Ohta et al., 2012; Dalton et al., 2013; Konôpková et al., 2016]. Measurements of MgSiO_3 bridgmanite (Mg-Bm) and post-perovskite were reported at pressures up to the CMB but at room temperature [Ohta et al., 2012]. However, to the best of our knowledge, the combined effects of chemical composition and pressure (e.g., the mass disorder of Fe and Al substitution) on the lattice thermal conductivity of Mg-Bm at lowermost mantle pressures have not been experimentally investigated, leading to an incomprehensive understanding of the thermal conductivity and heat transfer of this region. In this paper, we combine time domain thermorefectance and diamond anvil cell techniques to precisely measure the lattice thermal conductivity of Fe-bearing bridgmanite to 120 GPa. We then apply these results to model radial profiles in thermal conductivity throughout the lower mantle, lateral variations in thermal conductivity of LLSVPs, and heat flux across the CMB.

2. Experimental Details

2.1. Starting Materials and Sample Preparation

Chemically homogeneous single crystals of MgSiO_3 bridgmanite and (Fe,Al)-bearing bridgmanites were synthesized at 24 GPa and 1650–1760°C using a Kawai-type multianvil apparatus with a substantially long heating duration for large crystals to grow [Okuchi et al., 2015]. Chemical compositions of the (Fe,Al)-bearing bridgmanites were characterized by an electron probe microanalyzer and determined to be $\text{Mg}_{0.96}\text{Fe}_{0.07}\text{Si}_{0.98}\text{O}_3$ (Fe-Bm) and $\text{Mg}_{0.89}\text{Fe}_{0.12}\text{Al}_{0.11}\text{Si}_{0.89}\text{O}_3$ (Fe-Al-Bm) [Okuchi et al., 2015], where the Fe and Al contents are representative of those in the lower mantle pyrolite compositional model [Irifune et al., 2010]. Crystalline quality and lattice parameters of the samples from the same capsule were also evaluated using X-ray diffraction at GSECARS of the Advanced Photon Source [Mao et al., 2017]. Each of the bridgmanite crystals was polished down to a thickness of $\approx 10 \mu\text{m}$, coated with $\approx 80 \text{ nm}$ thick Al film and loaded, together with a small ruby ball, into a symmetric DAC with a culet size of 200 or 300 μm . The sample was then pressurized by loading silicone oil (CAS No. 63148-62-9 from ACROS ORGANICS) as the pressure medium, see Figure 1 for the schematic illustration of the sample geometry and experimental setup. The pressure was determined by ruby fluorescence [Mao et al., 1978], and the uncertainties of the pressure measurements were typically $< 5\%$.

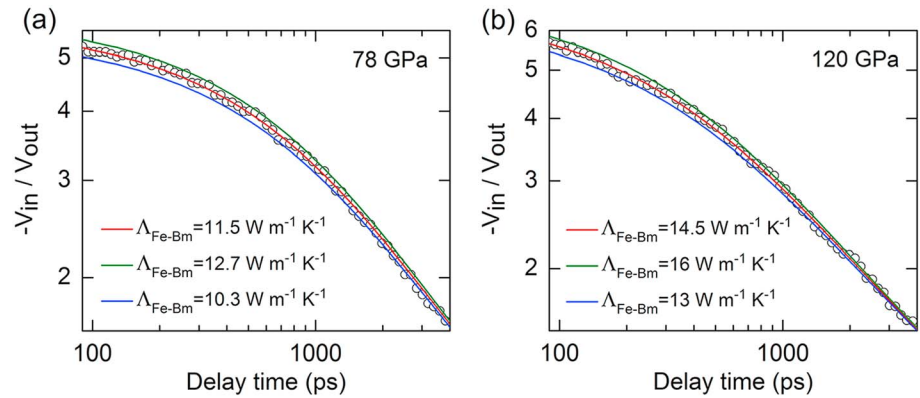


Figure 2. Comparison of example data with calculations by the thermal model for Fe-Bm crystal at high pressures. Example data for the ratio $-V_{in}/V_{out}$ as a function of delay time between pump and probe pulses are shown as open circles. The solid lines represent calculations by our bidirectional heat flow model with different values of Fe-Bm thermal conductivity Λ_{Fe-Bm} . At (a) 78 GPa and (b) 120 GPa, $\Lambda_{Fe-Bm} = 11.5$ and $14.5 \text{ W m}^{-1} \text{ K}^{-1}$, respectively, provide a best fit using parameters listed in Table 1. In our measurements, the ratio $-V_{in}/V_{out}$ has strong dependence on the Λ_{Fe-Bm} during delay time of few hundred picoseconds, e.g., 100 to 500 ps [Cahill and Watanabe, 2004; Zheng et al., 2007]. A 10% change in Λ_{Fe-Bm} shows a clear deviation from the best fit to the data, indicating that our thermal model fitting and derived Λ_{Fe-Bm} are precise and highly reliable due to the high-quality data and sample geometry.

2.2. High-Pressure Lattice Thermal Conductivity Measurements

After the pressure within the DAC equilibrated and reached a stable value, the lattice thermal conductivity of the bridgmanite was measured at room temperature using time domain thermoreflectance (TDTR). In the TDTR measurement, the output of a mode-locked Ti:sapphire oscillator laser was split into pump and probe beams. The pump beam heated the surface of Al film on the sample, creating temperature variations. The probe beam then detected the resulting changes in the optical reflectivity induced by the temperature changes on the Al film as a function of the time delayed between pump and probe beams. The in-phase V_{in} and out-of-phase V_{out} components of the variation of the reflected probe beam intensity, which were synchronous with the 8.7 MHz modulation frequency of the pump beam, were measured using a Si photodiode as well as an RF lock-in amplifier. The details of the TDTR are described elsewhere [Cahill, 2004; Kang et al., 2008].

The thermal conductivity of the bridgmanite was determined by comparing the time dependence of the ratio $-V_{in}/V_{out}$ to calculations based on a thermal model that takes into account heat flow into the sample substrate and into the pressure medium silicone oil [Ge et al., 2006; Schmidt et al., 2008]. Example data with calculations by the thermal model are shown in Figure 2. The thermal model contains several parameters—laser spot size (7.6 μm), thickness of Al film, thermal conductivity, and heat capacity of each layer—but the thermal conductivity of the bridgmanite sample is the only significant unknown and free parameter to be determined. Table 1 lists values of the thermal model parameters we used for the two sets of example data shown in Figure 2. Note that the ratio $-V_{in}/V_{out}$ at delay time of few hundred picoseconds is sensitive to and scales with the sum of thermal effusivity of bridgmanite and silicone oil divided by the heat capacity per unit area of Al film [Zheng et al., 2007]. The thickness of Al film at ambient pressure was measured in situ by picosecond acoustics, and estimates of the changes in Al thickness at high pressures were described in Chen et al. [2011]: Al thickness decreases by 12% at 25 GPa, by 18% at 60 GPa, and 21% at 120 GPa. Since the thermal penetration depths in the bridgmanite and silicone oil are on the order of hundreds of nanometers at the modulation frequency of the pump beam [Hsieh et al., 2009], the thermal model is insensitive to their thicknesses ($\sim 10 \mu\text{m}$) (see Figures S1a and S1b in the supporting information). Because the thermal conductivity of Al film at ambient pressure, $\approx 200 \text{ W m}^{-1} \text{ K}^{-1}$ [Zheng et al., 2007], is large and has no effect on the thermal model calculations (Figure S1c), we fix this value for thermal modeling at high pressures. We estimated the pressure dependence of Al heat capacity from data for the atomic density and elastic constants at high pressures along with calculations of Debye temperature, as described in Hsieh et al. [2009]. The thermal effusivity, square root of the product of thermal conductivity and volumetric heat capacity, of silicone oil at room temperature and up to 24 GPa were taken from Hsieh [2015]; for $P = 24$ to 123 GPa, the thermal effusivity was

Table 1. Input Parameters for the Bidirectional Heat Flow Model at Two Representative Pressures of 78 and 120 GPa^a

P (GPa)	$C_{\text{Fe-Bm}}$ ($\text{J cm}^{-3} \text{K}^{-1}$)	C_{Al} ($\text{J cm}^{-3} \text{K}^{-1}$)	h_{Al} (nm) ^b	$e = (\Lambda_{\text{Si}} C_{\text{Si}})^{1/2}$ ($\text{J m}^{-2} \text{K}^{-1} \text{s}^{-1/2}$)	r (μm)	$h_{\text{Fe-Bm/Si oil}}$ (μm)	Λ_{Al} ($\text{W m}^{-1} \text{K}^{-1}$)	G ($\text{MW m}^{-2} \text{K}^{-1}$)
78	3.39	2.68	77.7	2017	7.6	10	200	40
120	3.29	2.72	76.1	2260	7.6	10	200	300

^a $C_{\text{Fe-Bm}}$: Fe-Bm heat capacity, C_{Al} : Al heat capacity, h_{Al} : Al thickness, e : silicone oil thermal effusivity, r : laser spot size, $h_{\text{Fe-Bm/Si oil}}$: Fe-Bm thickness, $h_{\text{Si oil}}$: silicone oil thickness, Λ_{Al} : Al thermal conductivity, G : thermal conductance of Al/Fe-Bm and Al/silicone oil interfaces.

^bIn this experimental run, the Al thickness at ambient pressure is 96.3 nm.

estimated by extrapolation based on the data below 24 GPa that were fitted into a polynomial, assuming that the silicone oil remains in an amorphous phase at high pressures. Compared to the bridgmanite, the exceptionally low thermal effusivity of silicone oil at high pressures substantially reduces the uncertainty of deriving bridgmanite thermal conductivity as it has only minor effects, typically less than 10% uncertainty, on the thermal model calculations (see Figure S1d). This uncertainty is much smaller than the error propagated when using noble gases (Ar, Ne, He, etc., that solidify at high pressures) or solid pressure media whose thermal conductivities at high pressures are comparable or even larger than the samples.

The heat capacities of the Fe-Bm and Fe-Al-Bm at room temperature and high pressures are unknown. Since the contents of Fe and Al are relatively low, we assume that the pressure dependence of the heat capacities of Fe-Bm and Fe-Al-Bm is close to that of the Mg-Bm taken from Kiefer *et al.* [2002] and Tsuchiya *et al.* [2005]; the volumetric heat capacity $C = 3.4 \text{ J cm}^{-3} \text{ K}^{-1}$ at ambient pressure, $C = 3.51 \text{ J cm}^{-3} \text{ K}^{-1}$ at 30 GPa,

$C = 3.51 \text{ J cm}^{-3} \text{ K}^{-1}$ at 60 GPa, and $C = 3.3 \text{ J cm}^{-3} \text{ K}^{-1}$ at 123 GPa. We calculated the uncertainty in the thermal conductivity of the bridgmanites caused by uncertainty in each of the parameters used in our thermal model by evaluating the sensitivity of the thermal model to input parameters [see, e.g., Cahill and Watanabe, 2004; Zheng *et al.*, 2007; Hsieh, 2011]; details of the uncertainty evaluation on example tests are shown in Figure S1. We found that uncertainties in all the parameters propagate to $\approx 10\%$ error in the measured thermal conductivity of the bridgmanites before 30 GPa, $\approx 25\%$ error at 60 GPa, and $\approx 35\%$ error at 123 GPa.

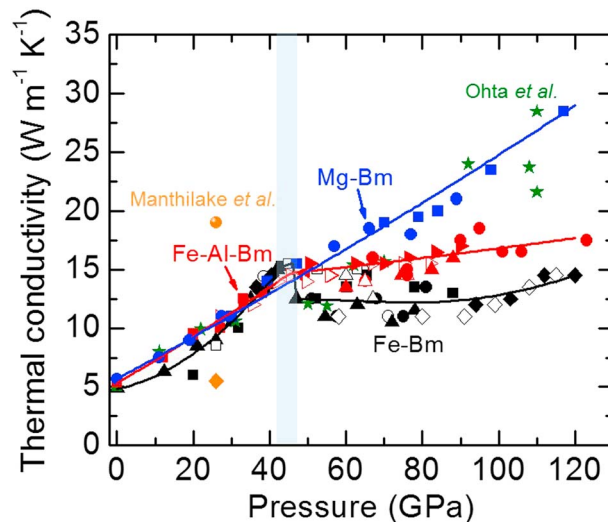


Figure 3. Lattice thermal conductivity of bridgmanite at high pressures and room temperature. Data for the Mg-Bm (blue symbols) are in good agreement with literature results [Ohta *et al.*, 2012] (green symbols). The thermal conductivities of Fe-Bm (black symbols) and Fe-Al-Bm (red symbols) are similar to Mg-Bm before $P \approx 40$ GPa, after which the conductivity of Fe-Bm decreases by $\approx 20\%$ and then increases slightly with pressure, whereas the conductivity of Fe-Al-Bm increases at a smaller rate with pressure. Each set of symbol shapes represents an individual measurement run, with solid symbols for compression and open symbols for the decompression cycle, respectively. The solid curves show fits to the data for each type of bridgmanite. Literature results for Mg-Bm (orange circle) and mixed with 3 mol % FeSiO_3 (orange diamond) at 26 GPa extrapolated to 300 K from [Manthilake *et al.*, 2011] are plotted for comparison. The light blue shading area indicates the pressure range where the pressure evolution of Fe-Bm and Fe-Al-Bm thermal conductivities changes drastically. The measurement uncertainties are $\approx 10\%$ before 30 GPa, $\approx 25\%$ at 60 GPa, and $\approx 35\%$ at 123 GPa.

3. Experimental Results

3.1. Thermal Conductivity of Mg-Bm, Fe-Bm, and Fe-Al-Bm

We precisely measured the lattice thermal conductivities of single-crystal Mg-Bm, Fe-Bm, and Fe-Al-Bm up to pressures near the lowermost mantle, where several seismic complexities are observed, including LLSVPs and the D'' discontinuity. The lattice thermal conductivity of single-crystal Mg-Bm (blue symbols in Figure 3) increases monotonically from $5.7 \text{ W m}^{-1} \text{ K}^{-1}$ at ambient pressure to $28.5 \text{ W m}^{-1} \text{ K}^{-1}$ at

117 GPa, in good agreement with literature data for polycrystalline Mg-Bm (green symbols in Figure 3) [Ohta *et al.*, 2012] and theoretical calculations [Dekura *et al.*, 2013; Stackhouse *et al.*, 2015].

As for Fe-bearing Bm, the measured thermal conductivity is similar to the MgSiO₃ end-member before $P \approx 40$ GPa (black symbols in Figure 3), showing that the effect of Fe substitution on the lattice thermal conductivity of Mg-Bm is small at lower pressures. This behavior is different from the Fe substitution effect on MgO periclase, which results in a significant reduction in thermal conductivity by a factor of ≈ 10 at ambient conditions and a much larger pressure dependence when normalized to an ambient value [see Goncharov *et al.*, 2015]. Upon further compression, the thermal conductivity of Fe-Bm abruptly decreases by $\approx 20\%$ around 40 to 45 GPa, after which the thermal conductivity increases slightly with pressure to $\approx 14.5 \text{ W m}^{-1} \text{ K}^{-1}$ at 120 GPa, smaller than that of Mg-Bm by a factor of ≈ 2 . Recent theoretical and experimental studies showed that the A-site iron ions of Bm lattice undergo an enhanced local lattice distortion with an extremely high hyperfine quadrupole value for Fe²⁺ in pressure ranges similar to our study [e.g., Hsu *et al.*, 2010; Mao *et al.*, 2017]. Although the occurrence of the intermediate-spin and low-spin transition of Fe²⁺ has been proposed, the consensus is that the A-site Fe²⁺ and Fe³⁺ remain in the high-spin state, while the B-site Fe³⁺ undergoes a high-spin to low-spin transition (see section 3.2). We thus attribute the reduced thermal conductivity around 40 to 45 GPa to the pressure-induced lattice distortion of A-site Fe²⁺ and Fe³⁺ in Fe-Bm, through which the phonon group velocity and phonon densities of states may have changed.

We now turn to the combined effects of Al and Fe substitution on the lattice thermal conductivity of Mg-Bm (red symbols in Figure 3). Again, the lattice thermal conductivity of (Fe,Al)-bearing Bm remains similar to that of Mg-Bm and Fe-Bm until $P \approx 40$ GPa, after which the conductivity increases in a smaller rate with pressure, and reaches $17.5 \text{ W m}^{-1} \text{ K}^{-1}$ at 123 GPa. The reduced slope with pressure suggests that the thermal conductivity of Fe-Al-Bm is sensitive to the slight changes in the phonon densities of states and group velocity induced by relatively minimal lattice distortion of A-site iron ions (see section 3.2) as well as the enhanced phonon-defect and phonon-boundary scatterings that would suppress the expected increase in the thermal conductivity at higher pressures.

3.2. Pressure-Induced Lattice Distortion in Fe-Bm and Fe-Al-Bm

The ferrous (Fe²⁺) and ferric (Fe³⁺) irons of our Fe-Bm crystal are both largely in the A-site of the perovskite lattice (pseudo-dodecahedral site) based on Mössbauer analysis of our samples, whereas a significant increase in the quadrupole splitting (QS) of Fe²⁺ occurs between 13 and 32 GPa [Mao *et al.*, 2017]. Such pressure-enhanced QS occurs along with abrupt changes in the bond length and tilting angle of the Fe-O octahedra, as well as in the spontaneous shear strain observed around 40 GPa, and has been attributed to an enhanced lattice distortion (Jahn-Teller effect) of the A-site Fe²⁺ in the high-spin state [Jackson *et al.*, 2005; Hsu *et al.*, 2010, 2011; Ballaran *et al.*, 2012; Lin *et al.*, 2013; Mao *et al.*, 2017]. Although the occurrence of the extremely high QS component at high pressures was also proposed to be caused by an electronic high-spin to intermediate-spin crossover [Lin *et al.*, 2008; McCammon *et al.*, 2008; Potapkin *et al.*, 2013], recent first-principles calculations [Bengtson *et al.*, 2009; Hsu and Wentzcovitch, 2014; Shukla *et al.*, 2015] show that the intermediate-spin state of Fe²⁺ is unlikely to occur in the lower mantle conditions. Moreover, equation of state measurements of the Fe-Bm in Mao *et al.* [2017] did not show an abrupt volume collapse up to 85 GPa, indicating the absence of a pressure-induced high-spin to low-spin crossover in B-site Fe³⁺ over the investigated pressure range. We therefore conclude that the reduction in our Fe-Bm lattice thermal conductivity observed around 40 to 45 GPa is likely due to the pressure-induced lattice distortion of A-site Fe²⁺ and Fe³⁺, through which the phonon densities of states as well as phonon group velocity may have been slightly altered.

In our Fe-Al-Bm crystals the Fe²⁺ and Fe³⁺ both occupy the A-site and stay in the high-spin state [Mao *et al.*, 2017] over the investigated pressure range. Recently, Lin *et al.* [2016] used X-ray emission, X-ray diffraction, and Mössbauer spectroscopy to study the spin and valence states of iron in the same Fe-Al-Bm sample as ours and did not observe any spin transition up to the pressures of the lowermost mantle. The decrease in the slope of the thermal conductivity with pressure around 40 GPa without a significant reduction as observed in Fe-Bm suggests that the pressure evolution of Fe-Al-Bm thermal conductivity is sensitive to the relatively minimal changes in phonon densities of states and group velocity resulted from the suppressed lattice distortion of A-site Fe²⁺ and Fe³⁺ in Fe-Al-Bm.

4. Thermal Conductivity Modeling for Earth's Lower Mantle

The critical influence of Fe substitution on the lattice thermal conductivity of bridgmanite at lowermost mantle revealed by our measurements provides novel insights into the thermo-chemical structure and dynamics of the lower mantle and the CMB heat flux. To quantify the influence of lateral variations in iron on lowermost mantle thermal conductivity, we performed data modeling where we considered the effects of variations in temperature, global iron content (dX_{Fe}), and volume fraction of bridgmanite (dX_{Bm}), as well as the influence of iron partitioning between bridgmanite and ferropericlasite, K_D [Badro, 2014].

4.1. Effect of Temperature

Temperature dependence of lower mantle minerals' thermal conductivities may be described following

$$\Lambda(T) \propto \frac{K}{T^n}, \quad (1)$$

where K is a parameter depending on the material, including its iron content (see below), but not on temperature, and $0.5 \leq n \leq 1.0$. In Mg-Bm, lattice thermal transport is predominantly operated through anharmonic three-phonon scattering; in (Fe,Al)-bearing bridgmanite, however, the three-phonon scattering dominates at low phonon frequency regime and the mass disorder effect plays a critical role at higher frequency regime. As a result, the temperature dependence of the mass disordered Fe-Bm and Fe-Al-Bm would change from a typical T^{-1} dependence to $T^{-1/2}$ dependence [Klemens *et al.*, 1962; Dalton *et al.*, 2013]. Such $T^{-1/2}$ dependence was also reported in other iron-bearing mantle minerals [Xu *et al.*, 2004]. Recent first-principles calculations by Stackhouse *et al.* [2015] indicate that the temperature dependence of Mg-Bm at deep lower mantle conditions is weaker than the typically assumed T^{-1} and $T^{-1/2}$ dependences due to the saturation effect. Stackhouse *et al.* [2015] showed a consistent Mg-Bm thermal conductivity with other calculations using the typical T^{-1} dependence [e.g., Dekura *et al.*, 2013; Tang *et al.*, 2014] at moderately high temperature but predicted a larger value at lowermost mantle conditions. For applications to lower mantle thermal conductivity and CMB heat flux (see below), we assumed $n = 0.5$ for Fe-Bm and Fe-Al-Bm. However, to evaluate the influence of n , we further performed a few calculations with $n = 1.0$. Table S1 in the supporting information shows that for $n = 1.0$, the thermal contribution to variations in thermal conductivity is enhanced by about a factor of 2, compared to $n = 0.5$. However, when compositional effects (section 4.2) are also taken into account, thermal conductivity anomalies obtained for $n = 0.5$ and $n = 1.0$ are very similar. Furthermore, the impact on CMB heat flux (section 5) is limited, with RMS in relative anomalies in heat flux being only $\sim 10\%$ larger for $n = 1.0$ than for $n = 0.5$ (Table S1).

Assuming that the temperature dependence of Mg-Bm follows the calculations in Stackhouse *et al.* [2015] and those of Fe-Bm and Fe-Al-Bm follow the $T^{-1/2}$ dependence, our new data enable lattice thermal conductivity estimation at relevant P - T conditions near the lowermost mantle (≈ 120 GPa and 3000 K): ≈ 9 W m^{-1} K^{-1} for Mg-Bm, 4.6 W m^{-1} K^{-1} for Fe-Bm, and 5.5 W m^{-1} K^{-1} for Fe-Al-Bm. Compared to available experimental data for the radiative thermal conductivity of (Fe,Al)-bearing bridgmanite with a similar chemical composition but large uncertainties [Goncharov *et al.*, 2008; Keppler *et al.*, 2008], ≈ 0.5 to 3 W m^{-1} K^{-1} , our results for the lattice thermal conductivity of (Fe,Al)-bearing bridgmanites at similar P - T conditions are larger, indicating that the lattice component majorly contributes to the heat transfer in Earth's deep lower mantle. Our findings here challenge previous models [e.g., Keppler *et al.*, 2008; Goncharov *et al.*, 2010] in which the thermal radiation mechanism was expected to be dominant.

Furthermore, deriving equation (1) allows estimating relative variations of thermal conductivity with temperature, which may be written

$$d \ln \Lambda^T = \frac{1}{\Lambda(T_{ref})} \frac{d\Lambda}{dT} dT = -n \frac{dT}{T_{ref}}, \quad (2)$$

where $dT = (T - T_{ref})$ is the lateral temperature anomaly compared to a reference temperature T_{ref} . For T_{ref} in the range of 3000–4000 K, which is typical of CMB temperature [e.g., Tackley, 2012], $dT = 500$ K [Trampert *et al.*, 2004; Mosca *et al.*, 2012], and $n = 0.5$, thermal conductivity decreases by about 6 to 8%, i.e., smaller than the compositional effect (section 4.2) by at least a factor of 5.

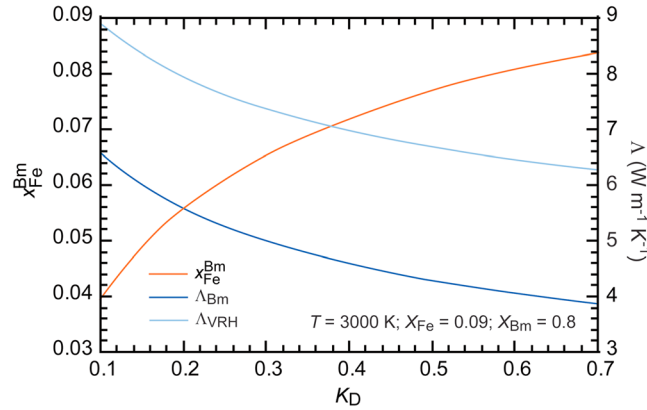


Figure 4. Iron fraction in bridgmanite, x_{Fe}^{Bm} , and thermal conductivity as a function of iron partitioning, K_D , and for temperature $T = 3000$ K, global fraction of iron $X_{Fe} = 0.09$, and volume fraction of bridgmanite $X_{Bm} = 0.8$. Λ_{Bm} is the thermal conductivity of bridgmanite and is calculated using equation (3) and the corresponding value of x_{Fe}^{Bm} and iron correction. Λ_{VRH} is the thermal conductivity of mantle aggregate calculated following the Voigt-Reuss-Hill average (equation (7)), with thermal conductivity of ferropericlase assumed to be independent of the iron content and fixed to $24 \text{ W m}^{-1} \text{ K}^{-1}$ (see text).

4.2. Effect of Composition

As demonstrated by our measurements, the thermal conductivity of bridgmanite at deep mantle pressures depends on the iron content, which may vary laterally in the deep mantle [Trampert *et al.*, 2004; Mosca *et al.*, 2012]. Assuming that the thermal conductivity of bridgmanite depends linearly on its iron content, x_{Fe}^{Bm} , it can be calculated using

$$\Lambda_{Bm}(x_{Fe}^{Bm}) = \Lambda_0 + ax_{Fe}^{Bm}, \quad (3)$$

where Λ_0 is the thermal conductivity for pure Mg-Bm and a is a constant that can be inferred from our measurements for Mg-Bm and Fe-bearing bridgmanites. At lowermost mantle pressure (120 GPa and higher) and ambient temperature, our new data indicate that $\Lambda_0 = 28.5 \text{ W m}^{-1} \text{ K}^{-1}$ and $\Lambda_{Bm}(x_{Fe}^{Bm} = 0.072) = 14.5 \text{ W m}^{-1} \text{ K}^{-1}$, leading to $a = -194.4 \text{ W m}^{-1} \text{ K}^{-1}$. At lower mantle

temperature, a correction should be performed: for $T = 3000$ K, and assuming that the temperature dependence of Mg-Bm follows the results in Stackhouse *et al.* [2015] and Fe-Bm takes $n = 0.5$ in equation (1), $\Lambda_0 = 9.0 \text{ W m}^{-1} \text{ K}^{-1}$ and $\Lambda_{Bm}(x_{Fe}^{Bm} = 0.072) = 4.6 \text{ W m}^{-1} \text{ K}^{-1}$, which leads to $a = -61.1 \text{ W m}^{-1} \text{ K}^{-1}$. From equation (3), one can define relative anomalies in thermal conductivity due to iron anomalies, with respect to a reference conductivity $\Lambda_{Bm,ref}$ taken at reference value $x_{Fe,ref}^{Bm}$

$$d \ln \Lambda_{Bm}^{Fe} = \frac{1}{\Lambda_{Bm,ref}} \frac{\partial \Lambda_{Bm}}{\partial x_{Fe}^{Bm}} dx_{Fe}^{Bm} = \frac{a}{\Lambda_{Bm,ref}} \left(\frac{T_0}{T_{ref}} \right)^n dx_{Fe}^{Bm} \quad (4)$$

where $dx_{Fe}^{Bm} = (x_{Fe}^{Bm} - x_{Fe,ref}^{Bm})$ is the excess iron in bridgmanite; $T_0 = 300$ K is the ambient temperature, at which our thermal conductivity measurements were conducted; and $a = -194.4 \text{ W m}^{-1} \text{ K}^{-1}$ the iron correction. The assumption that the thermal conductivity of bridgmanite varies linearly with x_{Fe}^{Bm} may become invalid if x_{Fe}^{Bm} is too large compared to that of our samples ($x_{Fe}^{Bm} = 0.072$). In particular, due to saturation effect, the thermal conductivity of bridgmanite may no longer be reduced for values of x_{Fe}^{Bm} larger than a threshold value. Importantly, in the lower mantle the fraction of iron in bridgmanite likely varies by only a few percent, remaining in the range of 0.05–0.10 (see next paragraphs and Figures 4 and S2), i.e., close to the iron content of our samples. It is therefore reasonable to assume that in the case of the lower mantle, the thermal conductivity of bridgmanite varies linearly with x_{Fe}^{Bm} . Finer modeling of the effect of iron on the thermal conductivity of bridgmanite would require additional experiments, e.g., for x_{Fe}^{Bm} around 0.05 and 0.1. In addition, the $T^{-1/2}$ dependence has been reported to reasonably well describe the temperature dependence of thermal conductivity of crystals mixed with impurities [see, e.g., Klemens *et al.*, 1962; Xu *et al.*, 2004; Dalton *et al.*, 2013], among which the crystals and contents of impurities are different from each other. This suggests that in our case, it is reasonable to assume that the effect of temperature is independent of the iron content, in particular when the variation of iron content in bridgmanite is small.

Variations of iron in the Earth's mantle are usually parameterized in terms of the global volume fraction of iron oxide (FeO), X_{Fe} , given by

$$X_{Fe} = X_{Bm}x_{Fe}^{Bm} + (1 - X_{Bm})x_{Fe}^{FP}, \quad (5)$$

where X_{Bm} is the volume fraction of bridgmanite in the aggregate and x_{Fe}^{Bm} and x_{Fe}^{FP} are the individual iron fractions in bridgmanite and ferropericlase. For given values of X_{Fe} and X_{Bm} , the iron fraction in

bridgmanite, $x_{\text{Fe}}^{\text{Bm}}$, can be obtained by prescribing the iron partitioning between bridgmanite (Mg,Fe)SiO₃ and ferropericlae (Mg,Fe)O,

$$K_D = \frac{x_{\text{Fe}}^{\text{Bm}} / (1 - x_{\text{Fe}}^{\text{Bm}})}{x_{\text{Fe}}^{\text{Fp}} / (1 - x_{\text{Fe}}^{\text{Fp}})}, \quad (6)$$

and by solving equations (5) and (6) (see Appendix A1). In the Earth's lower mantle, iron goes preferentially to ferropericlae, i.e., $K_D < 1$. High-pressure mineral physics experiments and ab initio calculations further indicate that its value is in the range of 0.1–0.5 [e.g., *Badro*, 2014]. As an example, the brown curve in Figure 4 plots the iron fraction in bridgmanite, $x_{\text{Fe}}^{\text{Bm}}$, as a function of the iron partitioning, and for $X_{\text{Bm}} = 0.8$ and $X_{\text{Fe}} = 0.09$, which are typical of Earth's average mantle. For these values, $x_{\text{Fe}}^{\text{Bm}}$ is equal to 0.056 and 0.072 for $K_D = 0.2$ and $K_D = 0.4$, respectively. Figure S2 plots variations of the iron fraction in bridgmanite, $dx_{\text{Fe}}^{\text{Bm}}$, as a function of variations in the global fraction of iron, dX_{Fe} , and in the volume fraction of bridgmanite, dX_{Bm} . The reference iron fraction, $x_{\text{Fe},\text{ref}}^{\text{Bm}}$, is taken at $X_{\text{Fe},\text{ref}} = 0.09$ and $X_{\text{Bm},\text{ref}} = 0.8$ (brown curve in Figure 4). An increase in the global iron fraction of 0.03 ($X_{\text{Fe}} = 0.12$) combined with an increase in the fraction of bridgmanite of 0.1 ($X_{\text{Bm}} = 0.9$), typical of the variations found in LLSVPs [*Trampert et al.*, 2004; *Mosca et al.*, 2012], leads to an excess of the iron fraction in bridgmanite of 0.039 ($x_{\text{Fe}}^{\text{Bm}} = 0.095$) for $K_D = 0.2$, and 0.036 ($x_{\text{Fe}}^{\text{Bm}} = 0.108$) for $K_D = 0.4$.

The thermal conductivity of the lower mantle may be estimated by averaging thermal conductivities of individual minerals constituting the mantle aggregate, according to the relative proportion of these minerals. Here we define mantle thermal conductivity with a Voigt-Reuss-Hill (VRH) average. VRH average is commonly used to calculate the thermo-elastic properties of mantle minerals and is defined as the average of arithmetic and harmonic means. For an aggregate composed of two minerals (in our case, bridgmanite and ferropericlae), the VRH average of thermal conductivity writes as

$$\Lambda_{\text{VRH}} = \frac{1}{2} \left[X_{\text{Bm}} \Lambda_{\text{Bm}} + (1 - X_{\text{Bm}}) \Lambda_{\text{Fp}} + \frac{\Lambda_{\text{Bm}} \Lambda_{\text{Fp}}}{(1 - X_{\text{Bm}}) \Lambda_{\text{Bm}} + X_{\text{Bm}} \Lambda_{\text{Fp}}} \right], \quad (7)$$

where Λ_{Bm} and Λ_{Fp} are the thermal conductivities of bridgmanite and ferropericlae, respectively. Note that for the electrical conductivity of a representative mantle aggregate, VRH average has been shown to be biased toward the upper Hashin-Shtrikman bound [e.g., *Khan and Shankland*, 2012; *Deschamps and Khan*, 2016], which is considered as the upper possible bound for a multiphase aggregate. Because the thermal conductivities of bridgmanite and ferropericlae differ by less than 1 order of magnitude (see discussion below), such bias might be limited and smaller than experimental uncertainties. Interestingly, preliminary calculations indicate that for thermal conductivity, VRH average is close to the geometric average of Hashin-Shtrikman bounds. The thermal conductivity of bridgmanite as a function of $x_{\text{Fe}}^{\text{Bm}}$ is calculated using equation (3), with $x_{\text{Fe}}^{\text{Bm}}$ being given by equation (A2). For the conductivity of ferropericlae, we used the data of *Goncharov et al.* [2015] for Mg_{0.9}Fe_{0.1}O extrapolated at 120 GPa and assumed that it does not depend on the iron content, leading to $\Lambda_{\text{Fp}} = 76 \text{ W m}^{-1} \text{ K}^{-1}$ at room temperature. We further assumed that the temperature dependence of ferropericlae conductivity is similar to that of Fe-bearing bridgmanite, with $n = 0.5$ in equation (1), leading to $\Lambda_{\text{Fp}} = 24 \text{ W m}^{-1} \text{ K}^{-1}$ at $T = 3000 \text{ K}$. Note that variations in the volume fraction of bridgmanite, X_{Bm} , induce changes in the aggregate thermal conductivity, Λ_{VRH} , directly through equation (7), and indirectly by partially controlling the fractions of iron in bridgmanite and ferropericlae. Relative variations in the mantle conductivity due to variations in the volume fraction of bridgmanite and in the global volume fraction of iron are obtained by deriving equation (7) with respect to X_{Bm} and X_{Fe} following

$$d \ln \Lambda_{\text{VRH}}^{\text{Bm}} = \frac{1}{\Lambda_{\text{VRH}}} \frac{\partial \Lambda_{\text{VRH}}}{\partial X_{\text{Bm}}} dX_{\text{Bm}} = \frac{(\Lambda_{\text{Bm}} - \Lambda_{\text{Fp}})}{2 \Lambda_{\text{VRH}}} \left\{ 1 + \frac{\Lambda_{\text{Bm}} \Lambda_{\text{Fp}}}{[(1 - X_{\text{Bm}}) \Lambda_{\text{Bm}} + X_{\text{Bm}} \Lambda_{\text{Fp}}]^2} \right\} dX_{\text{Bm}} + \frac{1}{\Lambda_{\text{VRH}}} \left(\frac{\partial \Lambda_{\text{VRH}}}{\partial \Lambda_{\text{Bm}}} \frac{\partial \Lambda_{\text{Bm}}}{\partial X_{\text{Bm}}} + \frac{\partial \Lambda_{\text{VRH}}}{\partial \Lambda_{\text{Fp}}} \frac{\partial \Lambda_{\text{Fp}}}{\partial X_{\text{Bm}}} \right) dX_{\text{Bm}}, \quad (8)$$

and

$$d \ln \Lambda_{\text{VRH}}^{\text{Fe}} = \frac{1}{\Lambda_{\text{VRH}}} \frac{\partial \Lambda_{\text{VRH}}}{\partial X_{\text{Fe}}} dX_{\text{Fe}} = \frac{1}{\Lambda_{\text{VRH}}} \left(\frac{\partial \Lambda_{\text{VRH}}}{\partial \Lambda_{\text{Bm}}} \frac{\partial \Lambda_{\text{Bm}}}{\partial X_{\text{Fe}}} + \frac{\partial \Lambda_{\text{VRH}}}{\partial \Lambda_{\text{Fp}}} \frac{\partial \Lambda_{\text{Fp}}}{\partial X_{\text{Fe}}} \right) dX_{\text{Fe}}, \quad (9)$$

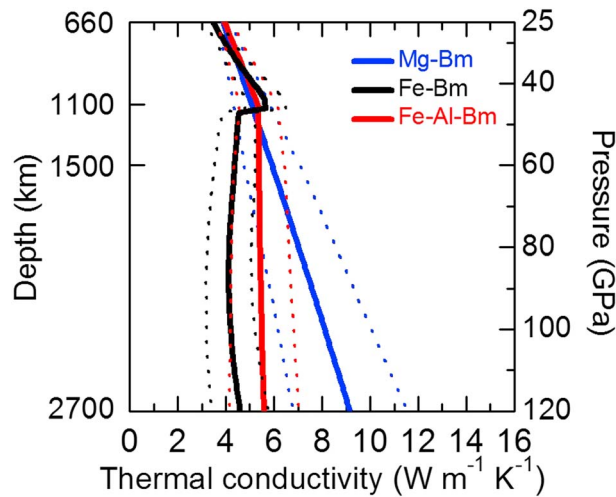


Figure 5. Profiles of the lattice thermal conductivity of bridgmanite along a model lower mantle geotherm (see section 4.3) with dotted curves showing uncertainties. These profiles are derived by extrapolating the room temperature data fits in Figure 3 to high temperature with respective temperature dependences described in the text.

$T_{\text{geotherm}}(\text{K}) = 2050 + (P-25) \times 10$, where P is in GPa. Note that variations of the extrapolated lattice thermal conductivity profiles in the lower mantle using other representative geotherms are relatively small and within the uncertainty of our modeled profiles shown in Figure 5. Along this geotherm, the thermal conductivity of Fe-Bm drops from ≈ 5.6 to $4.5 \text{ W m}^{-1} \text{ K}^{-1}$ around 45 GPa (≈ 1100 km depth), while the thermal conductivity of Mg-Bm continuously increases with increasing depth. The thermal conductivity of Fe-Bm is approximately half of the Mg-Bm at the lowermost mantle. Because bridgmanite is the most abundant mineral in the lower mantle, the sudden drop around 45 GPa and subsequent reduction of the thermal conductivity compared to Mg-Bm throughout the lower mantle are likely to induce a comparable reduction in the mantle thermal conductivity. Interestingly, tomographic images have shown that some (but not all) slabs are stacked around 1000 km [e.g., *Fukao and Obayashi, 2013*], which was recently attributed to an increase in viscosity in the depth range of 800–1200 km inferred from analysis of the long wavelengths of the geoid [*Rudolph et al., 2015*]. A sudden decrease in the thermal conductivity of Fe-Bm at mid-lower mantle depths, as suggested by our results, would, on the contrary, promote mantle flow, facilitating slabs crossing over the 1000 km barrier and sinking into the deeper mantle. Because the deviation of Fe-Bm thermal conductivity from the Mg-Bm substantially increases with depth, the descent of the subducted slabs in the lowermost mantle would be further accelerated. The decrease in the thermal conductivity, together with other effects that remain to be identified, may thus compensate the previously expected viscosity barrier at approximately 1000 km, and eventually allow slabs to reach the bottom of the mantle, as indicated by tomographic images. This scenario modifies our current view of the deep mantle dynamics and could be tested by numerical models of convection including, among other complexities, a depth-dependent thermal conductivity.

4.4. Lateral Variations in the Thermal Conductivity at the Lowermost Mantle

Figure 6a plots the relative variations in thermal conductivity of bridgmanite due to variations in iron, $d \ln \Lambda_{\text{Bm}}^{\text{Fe}}$ (equation (4)), as a function of the anomalies in the global iron content and volume fraction of bridgmanite, dX_{Fe} and dX_{Bm} , and for iron partitioning $K_D = 0.25$ (for other values of K_D , see Figure S3). For each iron partitioning, the reference value, $\Lambda_{\text{Bm,ref}}$, is calculated at $X_{\text{Fe,ref}} = 0.09$ and $X_{\text{Bm,ref}} = 0.8$ (dark blue curve in Figure 4). For $dX_{\text{Fe}} = 0.03$ and $dX_{\text{Bm}} = 0.1$, typical of the compositional anomalies that may be found in LLSVPs [*Trampert et al., 2004*], and for $K_D = 0.25$, the lattice thermal conductivity of Fe-bearing bridgmanite decreases by 45% compared to its reference value at $X_{\text{Fe}} = 0.09$ and $X_{\text{Bm}} = 0.8$.

We then calculated variations in the thermal conductivity of an aggregate (VRH average) of bridgmanite and ferropericase at temperature $T_{\text{ref}} = 3000$ K and lowermost mantle pressure, where the conductivity of

where partial derivatives involved in equations (8) and (9) are given in Appendix A2 (equations (A4) to (A9)). According to equation (3), $\partial \Lambda_{\text{Bm}} / \partial X_{\text{Fe}}^{\text{Bm}} = a(T_0/T_{\text{ref}})^n$, where $T_0 = 300$ K is the ambient temperature at which our thermal conductivity measurements were performed, and $a = -194.4 \text{ W m}^{-1} \text{ K}^{-1}$. Furthermore, since we assumed that the conductivity of ferropericase does not depend on the iron content, $\partial \Lambda_{\text{VRH}} / \partial X_{\text{Fe}}^{\text{FP}} = \partial \Lambda_{\text{FP}} / \partial X_{\text{Fe}}^{\text{FP}} = 0$.

4.3. Radial Profile of Lower Mantle Thermal Conductivity

Figure 5 shows profiles of the lattice thermal conductivity of bridgmanite along a model lower mantle geotherm, which we here define with a linear interpolation between P - T conditions at depths of 700 km (25 GPa, 2050 K) and 2620 km (120 GPa, 3000 K):

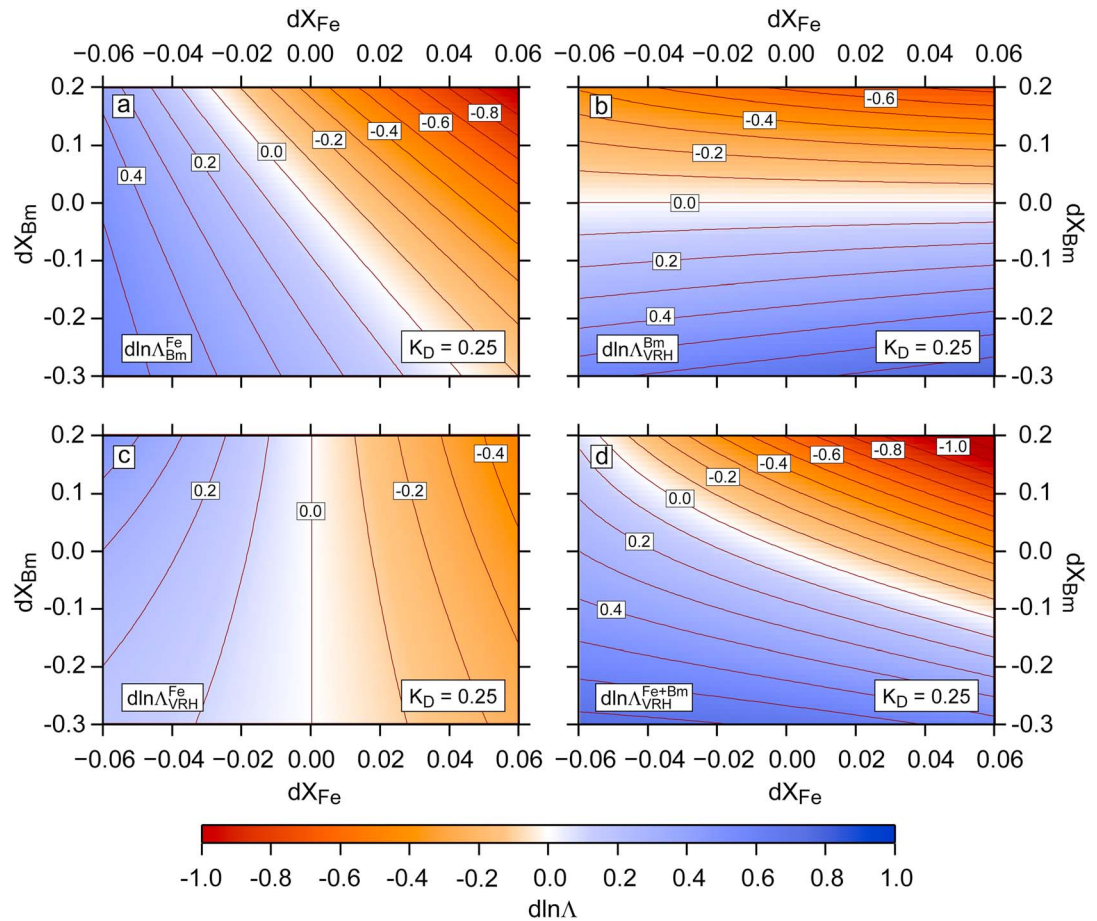


Figure 6. Relative variations in thermal conductivity (color scale) due to variations in global iron content, X_{Fe} , and volume fraction of bridgmanite, X_{Bm} . (a) Variations in bridgmanite conductivity, Λ_{Bm} , due to variations in iron fraction in bridgmanite, x_{Fe}^{Bm} (equation (4)). (b) Variations in conductivity of a bridgmanite-ferropericase aggregate (VRH average), Λ_{VRH} , due to variations in X_{Bm} (equation (8)). (c) Variations in Λ_{VRH} due to variations in X_{Fe} (equation (9)). (d) Variations in Λ_{VRH} due to combined variations in X_{Fe} and X_{Bm} . Reference values are $X_{Fe,ref} = 0.09$ and $X_{Bm,ref} = 0.8$, respectively, and iron partitioning, K_D , is equal to 0.25 (see Figures S3 and S4 for other values). Calculations are made at the lowermost mantle pressure, $P = 120$ GPa, and reference conductivities are shown in Figure 4.

ferropericase, $\Lambda_{Fp} = 24 \text{ W m}^{-1} \text{ K}^{-1}$, was extrapolated from recent experiments [Goncharov *et al.*, 2015]. Figures 6b–6d plot $d\ln\Lambda_{VRH}^{Bm}$ (equation (8)), $d\ln\Lambda_{VRH}^{Fe}$ (equation (9)), and their combined effect for iron partitioning $K_D = 0.25$ (for other values of K_D , see Figure S4). The total influence of X_{Bm} , including its effect on x_{Fe}^{Bm} , is larger than that of X_{Fe} alone and gets larger with decreasing iron partitioning. For $K_D = 0.25$, $dX_{Fe} = 0.03$, and $dX_{Bm} = 0.1$, the decrease in the aggregate thermal conductivity due to changes in iron and bridgmanite content reaches 21% and 30%, respectively. Importantly, the combined effect of X_{Bm} and X_{Fe} remains strong, with a reduction of conductivity slightly larger than 50% (Figure 6d). For comparison, the decrease in the lattice thermal conductivity due to a temperature anomaly of 500 K ranges between 6% and 8% depending on the reference temperature.

Finally, we calculated thermal conductivity anomalies associated with the thermo-chemical model from probabilistic tomography [Trampert *et al.*, 2004]. This thermo-chemical model of Earth’s mantle includes lateral variations in temperature, global iron (FeO) content, and volume fraction of bridgmanite (Figures 7a–7c). Updated models [Mosca *et al.*, 2012] include a finer radial parameterization and variations in post-perovskite at the bottom of the mantle. However, since we did not perform thermal conductivity measurements for this mineral, we preferred using Trampert *et al.* [2004] model. Note that thermo-chemical models derived from probabilistic tomography are limited to spherical harmonic degrees 2, 4, and 6. Following a scaling procedure based on the partitioning of odd and even degrees in classical tomography,

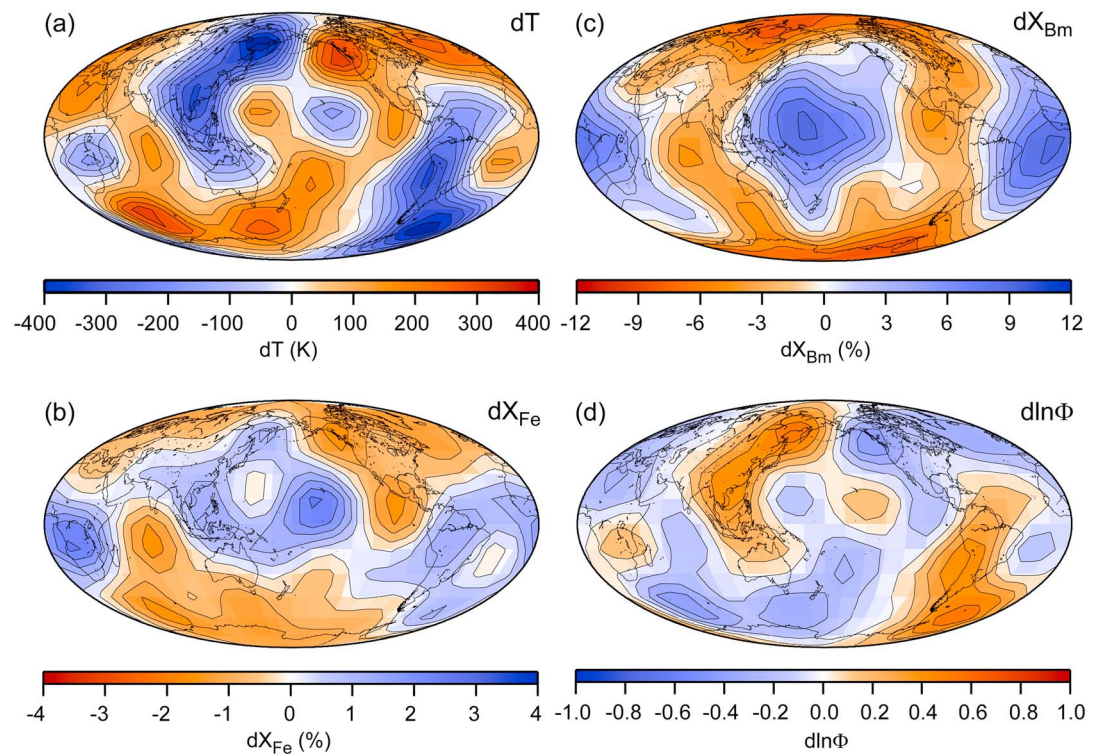


Figure 7. Distributions of anomalies in (a) temperature, (b) global iron content, and (c) volume fraction of bridgmanite derived from probabilistic tomography *Trampert et al.* [2004]. (d) CMB heat flux calculated from temperature anomalies in Figure 7a, and neglecting variations of thermal conductivity with temperature and composition, $d\ln\Phi = -dT/\Delta T_{ref}$, assuming $\Delta T_{ref} = 750$ K.

Amit et al. [2015] attempted recovering odd degrees of temperature distribution of *Mosca et al.* [2012] to build CMB heat flux. Interestingly, the resulting temperature pattern does not substantially differ from that containing even degrees only. Our calculations (Figures 8a–8c and Table 2) show that in LLSVPs, an excess in iron and bridgmanite leads to conductivity anomalies with a root-mean-square (RMS) amplitude of $\approx 15\%$ and a maximum decrease (increase) of up to 38% (24%). The thermal effect (Figure 8c) is smaller, with RMS amplitude anomalies of $\approx 3\%$. Such variations in lower mantle thermal conductivity may have important consequences for lower mantle dynamics. A decrease in the thermal conductivity of the constituting lower mantle materials, including bridgmanite, is expected to promote thermal convection in the region. Low thermal conductivity mapped in LLSVPs (Figures 8a–8c) would enhance internal flow within these regions and the generation of thermal plumes at the tops of these provinces. By contrast, if LLSVPs are not animated by convection, a lower thermal conductivity would reduce heat transfer and favor the heating up of LLSVPs.

An effect that is not accounted for in our thermal conductivity maps is the presence of post-perovskite. Experiments [*Ohta et al.*, 2012] reported that post-perovskite conductivity is larger than that of bridgmanite by about 60%. The amount and distribution of post-perovskite depend on the CMB temperature and on lateral variations in temperature. Based on our current understanding of the mineral physics and seismic properties, post-perovskite may be more likely present in D'' zones as patches extending up to about 200–300 km above the CMB, and outside the LLSVPs, usually considered to be hotter than surrounding regions. The possible presence of post-perovskite in D'' zones would then enhance the thermal conductivity contrast induced by variations in iron content predicted by our models (Figures 8a–8c).

In addition, our modeling of lower mantle thermal conductivity does not take into account the effect of radiative thermal conductivity. Given the limited available data with large uncertainty (≈ 0.5 to $3 \text{ W m}^{-1} \text{ K}^{-1}$) [*Goncharov et al.*, 2008; *Kepler et al.*, 2008], the radiative thermal conductivity of (Fe,Al)-bearing bridgmanite at expected lowermost mantle *P-T* conditions is approximately 10–60% of our results for the lattice thermal conductivity (≈ 4.6 and $5.5 \text{ W m}^{-1} \text{ K}^{-1}$; see Figure 5). As a result, the total thermal conductivity may be

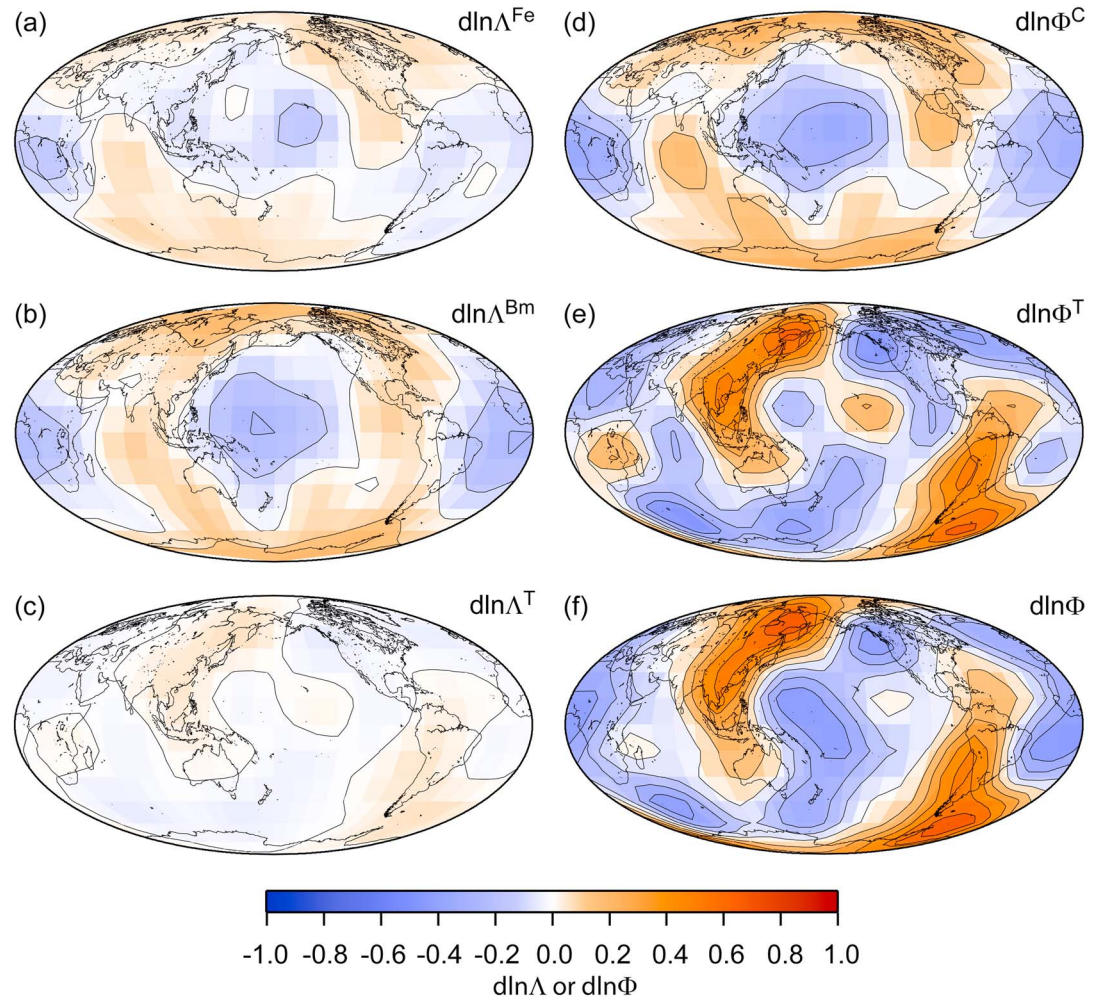


Figure 8. Relative variations in (a–c) thermal conductivity and (d–f) core-mantle boundary heat flux in the lowermost mantle (2000–2891 km). Thermal conductivity is obtained from the Voigt-Reuss-Hill (VRH) average of bridgmanite and ferropericlase. Figures 8a–8c show relative variations in conductivity due to global iron content ($d\ln\Lambda^{\text{Fe}}$, equation (9)), volume fraction of bridgmanite ($d\ln\Lambda^{\text{Bm}}$, equation (8)), and temperature ($d\ln\Lambda^{\text{T}}$, equation (2) with $n = 0.5$), respectively. Figures 8d and 8e map the relative heat flux anomalies due to variations in thermal conductivity with composition (third and fourth terms in the right-hand-side of equation (14)), and the relative heat flux anomalies due to variations in temperature and to their effects on conductivity (first and second terms in the right-hand-side of equation (14)). Figure 8f shows the total relative heat flux anomalies (equation (14)). Thermo-chemical distributions are from *Trampert et al.* [2004], iron partitioning is assumed to be constant, $K_D = 0.25$, reference thermochemical state is $X_{\text{Bm,ref}} = 0.8$, $X_{\text{Fe,ref}} = 0.09$, and $T_{\text{ref}} = 3000$ K, and CMB temperature $T_{\text{CMB}} = 3750$ K. Calculations are made at the lowermost mantle pressure, $P = 120$ GPa.

increased by approximately 10–60%, comparable to the uncertainty of our data ($\approx 35\%$) at lowermost mantle P - T conditions, when we take into account the radiative component. However, the effects of composition and temperature on the radiative thermal conductivity of (Fe,Al)-bearing bridgmanite have not been well characterized quantitatively. Sensitivity of radiative conductivity to temperature has an opposite trend to that of the lattice conductivity and may partially balance it, which would overall reduce the variations of thermal conductivity with temperature. The changes in both thermal conductivities induced by temperature anomaly at very high temperature condition of the lowermost mantle are expected to be relatively small, as suggested by Figure 8c. The compositional effect on the radiative conductivity is not well constrained, but assuming that its trend is similar to that on the lattice conductivity, we expect that the inclusion of radiative conductivity would only have minor influences on our modeling results. In particular, the decrease in the thermal conductivity of LLSVPs due to iron fraction anomaly would still be present, and the relative lateral variations of CMB heat flux pattern would be unchanged (see section 5).

Table 2. Root-Mean-Square (RMS), Minimum and Maximum in Thermo-chemical Distributions, Thermal Conductivity, and Heat Flux Relative Anomalies, and q^* Parameter^a

Quantity	RMS	Minimum	Maximum	q^*
Thermo-chemical Anomalies				
dT	182.61	-475.60	336.20	-
dX_{Bm}	0.0431	-0.0835	0.0926	-
dX_{Fe}	0.0098	-0.0182	0.0264	-
Thermal Conductivity Anomalies				
$d\ln\Lambda^{\text{Bm}}$	0.1058	-0.2528	0.1877	-
$d\ln\Lambda^{\text{Fe}}$	0.0558	-0.1744	0.0994	-
$d\ln\Lambda^T$	0.0304	-0.0560	0.0793	-
$d\ln\Lambda$	0.1455	-0.3784	0.2469	-
Heat Flux Anomalies				
$d\ln\Phi$ (Λ constant)	0.2435	-0.4483	0.6341	0.54
$d\ln\Phi^C = d\ln\Lambda^{\text{Bm}} + d\ln\Lambda^{\text{Fe}}$	0.1460	-0.3695	0.2210	0.30
$d\ln\Phi^T = -dT/\Delta T_{\text{ref}} + d\ln\Lambda^T$	0.2739	-0.5043	0.7134	0.61
$d\ln\Phi$	0.2943	-0.4921	0.7651	0.63

^aThermo-chemical anomalies are from *Trampert et al.* [2004]. Thermal conductivity anomalies due to changes in temperature ($d\ln\Lambda^T$), volume fraction of bridgmanite ($d\ln\Lambda^{\text{Bm}}$), and iron content ($d\ln\Lambda^{\text{Fe}}$) are given by equations (2), (8), and (9), respectively. For $d\ln\Lambda^T$, temperature exponent in equation (2) is set to $n = 0.5$. Heat flux variations due to anomalies in temperature ($d\ln\Phi^T$) are given by the sum of the first and second terms in the right-hand side of equation (14), $-dT(\varphi, \theta)/\Delta T_{\text{ref}} + d\ln\Lambda^T$, and heat flux variations due to anomalies in composition ($d\ln\Phi^C$) are given by the sum of the third and fourth terms, $d\ln\Lambda^{\text{Bm}} + d\ln\Lambda^{\text{Fe}}$. The CMB temperature is fixed to $T_{\text{CMB}} = 3750$ K, the reference temperature and composition are $T_{\text{ref}} = 3000$ K (leading to $\Delta T_{\text{ref}} = 750$ K), $X_{\text{Bm,ref}} = 0.8$, $X_{\text{Fe,ref}} = 0.09$, and the iron partitioning is set to $K_D = 0.25$. Calculations are made at lowermost mantle pressure, $P = 120$ GPa.

5. Implications for Heat Flux at the Core-Mantle Boundary

Variations in lowermost mantle thermal conductivities triggered by thermal and compositional changes may influence lateral variations in CMB heat flux and have implications for geodynamo. CMB heat flux is a key parameter controlling the extraction of heat from the core. Its amplitude and lateral variations may be used as a boundary condition for models of the geodynamo, thus influencing the outer core flow and the generated geomagnetic field. At a given longitude φ and latitude θ , the CMB heat flux is given by

$$\Phi(\varphi, \theta) = \Lambda(\varphi, \theta) \frac{[T_{\text{CMB}} - T(\varphi, \theta, D)]}{D}, \quad (10)$$

where the temperature at the CMB, T_{CMB} , is assumed constant, and T and Λ are the temperature and thermal conductivity at location φ , θ , and altitude D above the CMB. Physically, the value of D should be equal to the thickness of the thermal boundary layer at the bottom of the mantle, i.e., the region where the depth-increase of temperature is superadiabatic. This value is not well constrained but may reach a few hundreds of kilometers. Practically, because we are only mapping relative variations in heat flux, our heat flux maps do not depend on the value of D (equation (14)). It is, however, important to choose the temperature distribution not too close to CMB. The thermo-chemical model we use [*Trampert et al.*, 2004] samples the depth range of 2000–2891 km, and thus satisfies this requirement.

Both lateral variations in temperature and in thermal conductivity control lateral variations in CMB heat flux: increasing temperature decreases the vertical temperature gradient, and therefore reduces the heat flux; and heat flux decreases with thermal conductivity, which varies locally with temperature and with composition (see previous sections). Lateral variations in heat flux relative to a reference heat flux Φ_{ref} may be decomposed in variations due to anomalies in the radial temperature jump, ΔT , and anomalies in thermal conductivity, Λ , following

$$d\ln \Phi(\varphi, \theta) = \frac{1}{\Phi_{\text{ref}}} \left[\left(\frac{\partial \Phi}{\partial \Delta T} \right)_{\Lambda=\Lambda_{\text{ref}}} d\Delta T + \left(\frac{\partial \Phi}{\partial \Lambda} \right)_{\Delta T=\Delta T_{\text{ref}}} d\Lambda \right] = \frac{(\Delta T - \Delta T_{\text{ref}})}{\Delta T_{\text{ref}}} + d\ln \Lambda, \quad (11)$$

where Φ_{ref} is taken at reference temperature T_{ref} and reference thermal conductivity Λ_{ref} ,

$$\Phi_{\text{ref}} = \Lambda_{\text{ref}} \frac{[T_{\text{CMB}} - T_{\text{ref}}]}{D}. \quad (12)$$

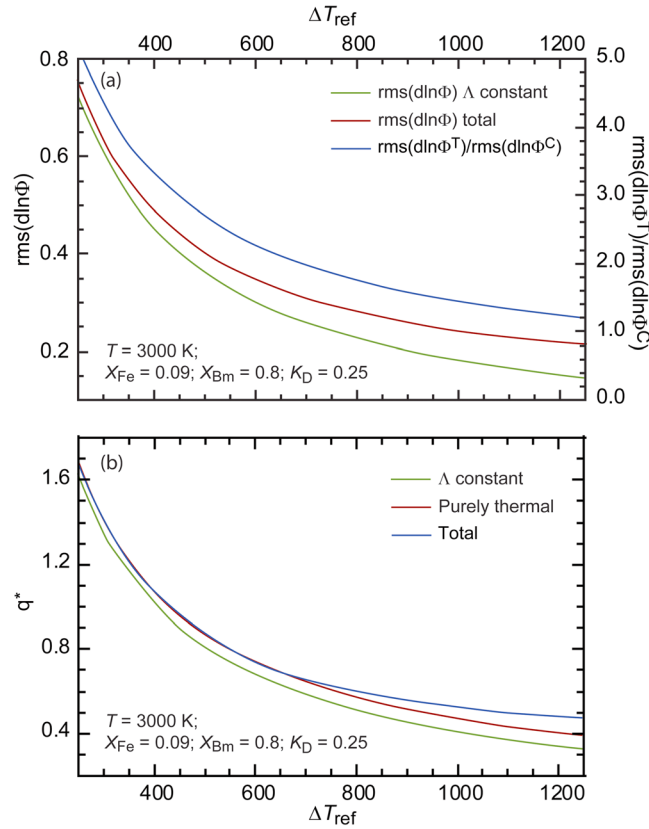


Figure 9. (a) Root-mean-square (RMS) in $d\ln\Phi$ (equation (14)) neglecting (green curve) and taking into account (red curve) lateral variations in thermal conductivity with temperature and composition. The blue curve plots the relative ratio between the RMS of thermal and compositional contributions to $d\ln\Phi$. Results are plotted as a function of the reference vertical temperature jump, ΔT_{ref} . (b) The q^* parameter (equation (15)) as a function of ΔT_{ref} for purely thermal contribution to the heat flux anomalies (red curve) and for thermal and compositional contributions (blue curve). For comparison, the green curve shows the q^* parameter obtained when neglecting the lateral variations in conductivity.

flux variations due to temperature variations alone, i.e., neglecting the variations in thermal conductivity. This contribution is mapped in Figure 7d, assuming $\Delta T_{ref} = 750$ K. Equation (14) requires the knowledge of the CMB temperature (T_{CMB}) and of the reference mantle geotherm (T_{ref}), which are both not well constrained. These values, or equivalently the value of ΔT_{ref} , are controlling the relative influence of heat flux variations due to temperature anomalies and its effect on thermal conductivity (given by the sum of the first and second terms in the right-hand-side of equation (14), $d\ln\Phi^T = -dT/\Delta T_{ref} + d\ln\Lambda^T$) and compositional anomalies (given by $d\ln\Phi^C = d\ln\Lambda^{Bm} + d\ln\Lambda^{Fe}$) (Figure 9a).

The results of our modeling for the Earth's lowermost mantle show that heat flux anomalies at the CMB are dominated by thermal effects (Figures 8d–8f and Table 2). For these calculations, we used, again, the bottom layer (2000–2891 km) of the 3-D thermo-chemical model from probabilistic tomography [Trampert *et al.*, 2004], iron partitioning $K_D = 0.25$, a reference thermo-chemical state defined by $X_{Bm,ref} = 0.8$, $X_{Fe,ref} = 0.09$, $T_{ref} = 3000$ K, and a CMB temperature $T_{CMB} = 3750$ K (leading to $\Delta T_{ref} = 750$ K). Table 2 lists root-mean-square (RMS) and minimum and maximum values of lateral relative variations in thermal conductivity and heat flux. Note that because the distributions in temperature and composition in Trampert *et al.* [2004] are not perfectly correlated, the relative anomalies $d\ln\Lambda^{Bm}$, $d\ln\Lambda^{Fe}$, and $d\ln\Lambda^T$ are also not correlated, and therefore, the sum of their RMS is different from the RMS of their sum. Figures 8d–8f and Table 2 indicate that heat flux variations are dominated by the thermal contribution, $d\ln\Phi^T$, with RMS 90% larger than that of the compositional contribution, $d\ln\Phi^C$. Comparison with Figure 7d further shows that heat flux maps are dominated directly

Noting that the radial temperature jump at a given location, ΔT , can be decomposed as

$$\Delta T(\varphi, \theta) = \Delta T_{ref} - dT(\varphi, \theta), \quad (13)$$

where $\Delta T_{ref} = (T_{CMB} - T_{ref})$ is the radial temperature jump at T_{ref} and $dT(\varphi, \theta)$ the lateral variation in temperature, and splitting $d\ln\Lambda$ in its thermal (equation (2)) and compositional (equations (8) and (9)) contributions, the lateral relative variations in heat flux can be written as the sum of lateral variations in temperature relative to the mean radial temperature jump, and lateral relative variations in thermal conductivity due to lateral changes in temperature and composition, i.e.,

$$d\ln\Phi(\varphi, \theta) = -\frac{dT(\varphi, \theta)}{\Delta T_{ref}} + d\ln\Lambda^T + d\ln\Lambda^{Bm} + d\ln\Lambda^{Fe}, \quad (14)$$

where dT is the temperature anomaly with respect to reference temperature T_{ref} , $\Delta T_{ref} = (T_{CMB} - T_{ref})$ is the mean radial temperature jump, T_{CMB} is the CMB temperature, and $d\ln\Lambda^T$, $d\ln\Lambda^{Bm}$, and $d\ln\Lambda^{Fe}$ are the relative conductivity anomalies due to variations in temperature, fraction of bridgmanite, and iron content, respectively. Note that the first term in the right-hand-side of equation (14), $-dT/\Delta T_{ref}$, represents the heat

by temperature anomalies, i.e., by the first term in the right-hand-side of equation (14). Including the effect of temperature on conductivity increases the amplitude of heat flux anomalies by $\sim 12\%$ but does not modify the heat flux pattern (Figure 8e). Taking into the effect of composition further increases the amplitude of heat flux anomalies by $\sim 7\%$ and slightly modifies the pattern (Figure 8f). In particular, iron and bridgmanite variations induce a substantial heat flux decrease within LLSVPs, with a local minimum up to 50% lower than the mean heat flux. Heat flux anomalies decrease in amplitude with increasing ΔT_{ref} (dark red curve in Figure 9a), due to the fact that Φ_{ref} increases with ΔT_{ref} . Furthermore, increasing ΔT_{ref} decreases $\ln\Phi^T$ but leaves $\ln\Phi^C$ unchanged; i.e., as ΔT_{ref} increases, the relative influence of compositional anomalies on heat flux becomes more important (blue curve in Figure 9a). The amplitude of $\ln\Phi$ only slightly depends on the iron partitioning, with RMS varying from 0.296 to 0.284 for K_D in the range of 0.1–0.7. For $\Delta T_{\text{ref}} = 750$ K, high heat flux anomalies, up to 70% larger than the mean heat flux, appear in regions where temperature is lower than average.

Amplitude and pattern of CMB heat flux anomalies may partially control the dynamics of the core. Dynamo actions may be lost if CMB heat flux variations are too high [Olson and Christensen, 2002]. The level of heat flux heterogeneity and its influence on the core dynamics are usually quantified with the q^* parameter, defined as

$$q^* = \frac{(\Phi_{\text{max}} - \Phi_{\text{min}})}{2\Phi_{\text{ref}}}, \quad (15)$$

which may also be written $q^* = (\ln\Phi_{\text{max}} - \ln\Phi_{\text{min}})/2$. Again, q^* strongly depends on the mean vertical temperature jump ΔT_{ref} (Figure 9b), and very slightly on the iron partitioning, K_D . For $K_D = 0.25$, our calculations indicate that q^* is equal to ≈ 0.63 for $\Delta T_{\text{ref}} = 750$ K and drops to ≈ 0.47 for $\Delta T_{\text{ref}} = 1250$ K. Furthermore, it is interesting to note that q^* is mainly controlled by the thermal contribution to heat flux anomalies (red curve in Figure 9b) and more particularly by the direct effect of temperature anomalies (green curve in Figure 9b). For instance, at $\Delta T_{\text{ref}} = 750$ K, q^* is equal to 0.54 if thermal conductivity is assumed constant, 0.61 if changes in conductivity due to changes in temperature are taken into account, and 0.63 if changes in conductivity induced by both thermal and compositional anomalies are included. The compositional contribution increases substantially q^* only for ΔT_{ref} larger than 700 K.

The values of q^* predicted by our modeling are usually considered as high enough to significantly alter geodynamo. There is, however, no consensus on the level of heterogeneity needed to affect the geodynamo. Values of $q^* > 1$ have been reported for successful dynamos [Dietrich and Wicht, 2013], in contradiction with earlier estimates [Olson and Christensen, 2002]. Heat flux pattern derived from classical tomography is dominated by Y_2^2 spherical harmonic terms and recovers well the locations of high-latitude intense geomagnetic flux patches on the CMB [Gubbins et al., 2007]. Refined patterns with equatorially concentrated heat flux allow explaining low-latitude intense geomagnetic flux patches [Amit et al., 2015]. In our model, the compositional contribution to CMB heat flux is dominated by a Y_2^2 pattern with local highs along the equator (Figure 8d). However, due to temperature distribution in [Trampert et al., 2004], the total heat flux map substantially deviates from a Y_2^2 pattern (Figure 8f). A potential consequence is the concentration of magnetic field lines in regions where CMB heat flux is high, which, in our maps, are located north of Japan and at the southern tip of South-America. Note that these regions of high heat flux are imposed by the pattern of temperature anomalies (Figure 7a) and already appear on the heat flux built with constant thermal conductivity (Figure 7d).

6. Conclusions

In this study, we have measured the lattice thermal conductivity of Fe-bearing and (Fe,Al)-bearing bridgmanites to pressures near the lowermost mantle. We found that the thermal conductivity of Fe-bearing bridgmanite initially increases monotonically with pressure but drops significantly around 45 GPa due to the pressure-induced lattice distortion on iron sites, making the thermal conductivity at the lowermost mantle conditions twice smaller than previously thought. Our experiments and modeling underline the strong effect of iron on the thermal conductivity of bridgmanite at lowermost mantle and its impact on CMB heat flux. A more detailed description of lower mantle thermal conductivity and CMB heat flux, however, requires additional experiments, including simultaneous high P - T measurements on the lattice and radiative thermal conductivity of the (Fe,Al)-bearing bridgmanite, ferropericline, and post-perovskite. This would in turn provide a better description of the lower mantle dynamics and new constraints for geodynamo models and associated magnetic field patterns.

Appendix A

A1. Individual Fraction of Iron in Bridgmanite and Ferropericlasite

The individual fraction of iron in bridgmanite and ferropericlasite, $x_{\text{Fe}}^{\text{Bm}}$ and $x_{\text{Fe}}^{\text{Fp}}$, may be calculated from the global fraction of iron, X_{Fe} , and the fraction of bridgmanite in the aggregate, X_{Bm} , and of the iron partitioning between bridgmanite and ferropericlasite, K_D (equation (6)). Following equation (5), $x_{\text{Fe}}^{\text{Fp}}$ may be expressed as

$$x_{\text{Fe}}^{\text{Fp}} = \frac{X_{\text{Fe}} - X_{\text{Bm}}x_{\text{Fe}}^{\text{Bm}}}{(1 - X_{\text{Bm}})}. \quad (\text{A1})$$

Replacing $x_{\text{Fe}}^{\text{Fp}}$ in equation (6) with its expression in equation (A1) defines a second-order polynomial in $x_{\text{Fe}}^{\text{Bm}}$, whose positive solution is

$$x_{\text{Fe}}^{\text{Bm}} = \frac{1 + (X_{\text{Bm}} + X_{\text{Fe}})(K_D - 1) - \sqrt{[1 + (X_{\text{Bm}} + X_{\text{Fe}})(K_D - 1)]^2 - 4X_{\text{Bm}}(K_D - 1)K_DX_{\text{Fe}}}}{2X_{\text{Bm}}(K_D - 1)}. \quad (\text{A2})$$

A similar procedure leads to

$$x_{\text{Fe}}^{\text{Fp}} = -\frac{1 + (X_{\text{Bm}} - X_{\text{Fe}})(K_D - 1) - \sqrt{[1 + (X_{\text{Bm}} - X_{\text{Fe}})(K_D - 1)]^2 + 4(1 - X_{\text{Bm}})(K_D - 1)X_{\text{Fe}}}}{2(1 - X_{\text{Bm}})(K_D - 1)}. \quad (\text{A3})$$

A2. Relative Anomalies in Thermal Conductivity Due to Changes in the Fractions of Iron and Bridgmanite

Relative variations in thermal conductivity of an aggregate of bridgmanite and ferropericlasite (Δ_{VRH}) due to variations in the global fraction in iron (X_{Fe}) and in the fraction of bridgmanite (X_{Bm}) are given by equations (8) and (9), assuming that the thermal conductivity of the aggregate is described by the Voigt-Reuss-Hill average of the thermal conductivities of bridgmanite (Λ_{Bm}) and ferropericlasite (Λ_{Fp}). Equations (8) and (9) involve partial derivatives of Δ_{VRH} with respect to Λ_{Bm} and Λ_{Fp} , and partial derivatives of Λ_{Bm} and Λ_{Fp} , with respect to X_{Fe} and X_{Bm} . These partial derivatives are listed below in equations (A4) to (A9).

$$\frac{\partial \Delta_{\text{VRH}}}{\partial \Lambda_{\text{Bm}}} = \frac{1}{2} X_{\text{Bm}} \left\{ 1 + \frac{\Lambda_{\text{Fp}}^2}{[(1 - X_{\text{Bm}})\Lambda_{\text{Bm}} + X_{\text{Bm}}\Lambda_{\text{Fp}}]^2} \right\} \quad (\text{A4})$$

$$\frac{\partial \Delta_{\text{VRH}}}{\partial \Lambda_{\text{Fp}}} = \frac{1}{2} (1 - X_{\text{Bm}}) \left\{ 1 + \frac{\Lambda_{\text{Bm}}^2}{[(1 - X_{\text{Bm}})\Lambda_{\text{Bm}} + X_{\text{Bm}}\Lambda_{\text{Fp}}]^2} \right\} \quad (\text{A5})$$

$$\frac{\partial \Lambda_{\text{Bm}}}{\partial X_{\text{Bm}}} = \frac{1}{2X_{\text{Bm}}} \left[1 - 2x_{\text{Fe}}^{\text{Bm}} - \frac{(1 - X_{\text{Bm}}) + K_DX_{\text{Bm}} - X_{\text{Fe}}(K_D + 1)}{\sqrt{[1 + (X_{\text{Bm}} + X_{\text{Fe}})(K_D - 1)]^2 - 4X_{\text{Bm}}(K_D - 1)K_DX_{\text{Fe}}}} \right] \frac{\partial \Lambda_{\text{Bm}}}{\partial x_{\text{Fe}}^{\text{Bm}}} \quad (\text{A6})$$

$$\frac{\partial \Lambda_{\text{Fp}}}{\partial X_{\text{Bm}}} = -\frac{1}{2(1 - X_{\text{Bm}})} \left[1 - 2x_{\text{Fe}}^{\text{Fp}} - \frac{(1 - X_{\text{Bm}}) + K_DX_{\text{Bm}} - X_{\text{Fe}}(K_D + 1)}{\sqrt{[1 + (X_{\text{Bm}} - X_{\text{Fe}})(K_D - 1)]^2 + 4X_{\text{Fe}}(1 - X_{\text{Bm}})(K_D - 1)}} \right] \frac{\partial \Lambda_{\text{Fp}}}{\partial x_{\text{Fe}}^{\text{Fp}}} \quad (\text{A7})$$

$$\frac{\partial \Lambda_{\text{Bm}}}{\partial X_{\text{Fe}}} = \frac{1}{2X_{\text{Bm}}} \left[1 - \frac{(1 - X_{\text{Bm}}) - K_DX_{\text{Bm}} + X_{\text{Fe}}(K_D - 1)}{\sqrt{[1 + (X_{\text{Bm}} + X_{\text{Fe}})(K_D - 1)]^2 - 4X_{\text{Bm}}(K_D - 1)K_DX_{\text{Fe}}}} \right] \frac{\partial \Lambda_{\text{Bm}}}{\partial x_{\text{Fe}}^{\text{Bm}}} \quad (\text{A8})$$

$$\frac{\partial \Lambda_{\text{Fp}}}{\partial X_{\text{Fe}}} = -\frac{1}{2(1 - X_{\text{Bm}})} \left[1 + \frac{(1 - X_{\text{Bm}}) - K_DX_{\text{Bm}} + X_{\text{Fe}}(K_D - 1)}{\sqrt{[1 + (X_{\text{Bm}} - X_{\text{Fe}})(K_D - 1)]^2 + 4X_{\text{Fe}}(1 - X_{\text{Bm}})(K_D - 1)}} \right] \frac{\partial \Lambda_{\text{Fp}}}{\partial x_{\text{Fe}}^{\text{Fp}}} \quad (\text{A9})$$

Acknowledgments

The work by W.P.H. and F.D. was supported by the Academia Sinica and the Ministry of Science and Technology of Taiwan, Republic of China, under contract CDA-106-M02, MOST 103-2112-M-001-001-MY3, 105-2116-M-001-024 (W.P.H.), and AS-102-CDA-M02 (F.D.). We thank J. Yang for the help with preparing the samples and Han Hsu and Stephen Stackhouse, Hagay Amit, and Laura Cobden for their helpful discussion and comments on the manuscript. J.F. Lin acknowledges support from the Geophysics and CSED1 Programs of the U.S. National Science Foundation, the Visiting Professorship Program of the Institute for Study of the Earth's Interior, Okayama University, and HPSTAR Center. J.F. Lin also acknowledges support and constructive discussion from the Cutting-Edge Research Club of the National Cheng Kung University (NCKU). This work was supported in part by JSPS KAKENHI (26287135). X-ray diffraction patterns of the crystal were analyzed at GeoSoilEnviroCARS sector of the APS. GSECARS was supported by the National Science Foundation (EAR-0622171) and Department of Energy (DE-FG02-94ER14466) under contract DE-AC02-06CH11357. APS is supported by 263 DOE-BES, under contract DE-AC02-06CH11357. We note that there are no data sharing issues since all of the experimental data and numerical modeling are provided in the figures and tables obtained by methods described in the text. The data shown in the figures and tables are available by contacting the corresponding authors upon request.

References

- Amit, H., F. Deschamps, and G. Choblet (2015), Numerical dynamos with outer boundary heat flux inferred from probabilistic tomography—Consequences for latitudinal distribution of magnetic flux, *Geophys. J. Int.*, *203*, 840–855, doi:10.1093/gji/ggv332.
- Ammann, M. W., A. M. Walker, S. Stackhouse, J. Wookey, A. M. Forte, J. P. Brodholt, and D. P. Dobson (2014), Variation of thermal conductivity and heat flux at the Earth's core mantle boundary, *Earth Planet. Sci. Lett.*, *390*, 175–185, doi:10.1016/j.epsl.2014.01.009.
- Badro, J. (2014), Spin transitions in mantle minerals, *Annu. Rev. Earth Planet. Sci.*, *42*, 231–248, doi:10.1146/annurev-earth-042711-105304.
- Ballaran, T. B., A. Kurnosov, K. Glazyrin, D. J. Frost, M. Merlini, M. Hanfland, and R. Caracas (2012), Effect of chemistry on the compressibility of silicate perovskite in the lower mantle, *Earth Planet. Sci. Lett.*, *333–334*, 181–190, doi:10.1016/j.epsl.2012.03.029.
- Bengtson, A., J. Li, and D. Morgan (2009), Mossbauer modeling to interpret the spin state of iron in (Mg,Fe)SiO₃ perovskite, *Geophys. Res. Lett.*, *36*, L15301, doi:10.1029/2009GL038340.
- Buffett, B. (2000), Earth's Core and the Geodynamo, *Science*, *288*(5473), 2007–2012, doi:10.1126/science.288.5473.2007.
- Cahill, D. G. (2004), Analysis of heat flow in layered structures for time-domain thermoreflectance, *Rev. Sci. Instrum.*, *75*(12), 5119–5122, doi:10.1063/1.1819431.
- Cahill, D. G., and F. Watanabe (2004), Thermal conductivity of isotopically pure and Ge-doped Si epitaxial layers from 300 to 550 K, *Phys. Rev. B*, *70*(23), 235322, doi:10.1103/PhysRevB.70.235322.
- Chen, B., W.-P. Hsieh, D. G. Cahill, D. R. Trinkle, and J. Li (2011), Thermal conductivity of compressed H₂O to 22 GPa: A test of the Leibfried-Schlömann equation, *Phys. Rev. B*, *83*(13), 132301, doi:10.1103/PhysRevB.83.132301.
- Cobden, L., C. Thomas, and J. Trampert (2015), Seismic detection of post-perovskite inside the Earth, in *The Earth Heterogeneous Mantle*, edited by A. Khan and F. Deschamps, pp. 391–440, Springer.
- Dalton, D. A., W.-P. Hsieh, G. T. Hohensee, D. G. Cahill, and A. F. Goncharov (2013), Effect of mass disorder on the lattice thermal conductivity of MgO periclase under pressure, *Sci. Rep.*, *3*, 2400, doi:10.1038/srep02400.
- Dekura, H., T. Tsuchiya, and J. Tsuchiya (2013), Ab initio lattice thermal conductivity of MgSiO₃ perovskite as found in Earth's lower mantle, *Phys. Rev. Lett.*, *110*, 25904, doi:10.1103/PhysRevLett.110.025904.
- Deschamps, F., and A. Khan (2016), Electrical conductivity as a constraint on lower mantle thermo-chemical structure, *Earth Planet. Sci. Lett.*, *450*, 108–119, doi:10.1016/j.epsl.2016.06.027.
- Deschamps, F., L. Cobden, and P. J. Tackley (2012), The primitive nature of large low shear-wave velocity provinces, *Earth Planet. Sci. Lett.*, *349–350*, 198–208, doi:10.1016/j.epsl.2012.07.012.
- Dietrich, W., and J. Wicht (2013), A hemispherical dynamo model: Implications for the Martian crustal magnetization, *Phys. Earth Planet. Inter.*, *217*, 10–21, doi:10.1016/j.pepi.2013.01.001.
- Fukao, Y., and M. Obayashi (2013), Subducted slabs stagnant above, penetrating through, and trapped below the 660 km discontinuity, *J. Geophys. Res. Solid Earth*, *118*, 5920–5938, doi:10.1002/2013JB010466.
- Garnero, E. J., and A. K. McNamara (2008), Structure and dynamics of Earth's lower mantle, *Science*, *320*, 626–628.
- Ge, Z., D. Cahill, and P. Braun (2006), Thermal conductance of hydrophilic and hydrophobic interfaces, *Phys. Rev. Lett.*, *96*(18), 186101, doi:10.1103/PhysRevLett.96.186101.
- Goncharov, A. F., B. D. Haugen, V. V. Struzhkin, P. Beck, and S. D. Jacobsen (2008), Radiative conductivity in the Earth's lower mantle, *Nature*, *456*(7219), 231–234, doi:10.1038/nature07412.
- Goncharov, A. F., V. V. Struzhkin, J. A. Montoya, S. Kharlamova, R. Kundargi, J. Siebert, J. Badro, D. Antonangeli, F. J. Ryerson, and W. Mao (2010), Effect of composition, structure, and spin state on the thermal conductivity of the Earth's lower mantle, *Phys. Earth Planet. Inter.*, *180*(3–4), 148–153, doi:10.1016/j.pepi.2010.02.002.
- Goncharov, A. F., S. S. Lobanov, X. Tan, G. T. Hohensee, D. G. Cahill, J.-F. Lin, S.-M. Thomas, T. Okuchi, and N. Tomioka (2015), Experimental study of thermal conductivity at high pressures: Implications for the deep Earth's interior, *Phys. Earth Planet. Inter.*, *247*, 11–16, doi:10.1016/j.pepi.2015.02.004.
- Gubbins, D., A. P. Willis, and B. Sreenivasan (2007), Correlation of Earth's magnetic field with lower mantle thermal and seismic structure, *Phys. Earth Planet. Inter.*, *162*(3–4), 256–260, doi:10.1016/j.pepi.2007.04.014.
- Haigis, V., M. Salanne, and S. Jahn (2012), Thermal conductivity of MgO, MgSiO₃ perovskite and post-perovskite in the Earth's deep mantle, *Earth Planet. Sci. Lett.*, *355–356*, 102–108, doi:10.1016/j.epsl.2012.09.002.
- Hofmeister, A. M. (1999), Mantle values of thermal conductivity and the geotherm from phonon lifetimes, *Science*, *283*(5408), 1699–1706, doi:10.1126/science.283.5408.1699.
- Hsieh, W.-P. (2011), Testing theories for thermal transport using high pressure, PhD dissertation, Univ. of Illinois, Urbana-Champaign, 28 pp.
- Hsieh, W.-P. (2015), Thermal conductivity of methanol-ethanol mixture and silicone oil at high pressures, *J. Appl. Phys.*, *117*(23), 235901, doi:10.1063/1.4922632.
- Hsieh, W.-P., B. Chen, J. Li, P. Keblinski, and D. G. Cahill (2009), Pressure tuning of the thermal conductivity of the layered muscovite crystal, *Phys. Rev. B*, *80*(18), 180302, doi:10.1103/PhysRevB.80.180302.
- Hsu, H., and R. M. Wentzcovitch (2014), First-principles study of intermediate-spin ferrous iron in the Earth's lower mantle, *Phys. Rev. B*, *90*, 195205, doi:10.1103/PhysRevB.90.195205.
- Hsu, H., K. Umamoto, P. Blaha, and R. M. Wentzcovitch (2010), Spin states and hyperfine interactions of iron in (Mg,Fe)SiO₃ perovskite under pressure, *Earth Planet. Sci. Lett.*, *294*(1–2), 19–26, doi:10.1016/j.epsl.2010.02.031.
- Hsu, H., P. Blaha, M. Cococcioni, and R. M. Wentzcovitch (2011), Spin-state crossover and hyperfine interactions of ferric iron in MgSiO₃ perovskite, *Phys. Rev. Lett.*, *106*(11), 118501, doi:10.1103/PhysRevLett.106.118501.
- Irfune, T., T. Shinmei, C. A. McCammon, N. Miyajima, D. C. Rubie, and D. J. Frost (2010), Iron partitioning and density changes of pyrolite in Earth's lower mantle, *Science*, *327*(5962), 193–195, doi:10.1126/science.1181443.
- Jackson, J. M., W. Sturhahn, G. Shen, J. Zhao, M. Y. Hu, D. Errandonea, J. D. Bass, and Y. Fei (2005), A synchrotron Mossbauer spectroscopy study of (Mg,Fe)SiO₃ perovskite up to 120 GPa, *Am. Mineral.*, *90*(1), 199–205, doi:10.2138/am.2005.1633.
- Kang, K., Y. K. Koh, C. Chiriac, X. Zheng, and D. G. Cahill (2008), Two-tint pump-probe measurements using a femtosecond laser oscillator and sharp-edged optical filters, *Rev. Sci. Instrum.*, *79*(11), 114901, doi:10.1063/1.3020759.
- Keppler, H., L. S. Dubrovinsky, O. Narygina, and I. Kantor (2008), Optical absorption and radiative thermal conductivity of silicate perovskite to 125 GPa, *Science*, *322*, 1529–1532.
- Khan, A., and T. J. Shankland (2012), A geophysical perspective on mantle water content and melting: Inverting electromagnetic sounding data using laboratory-based electrical conductivity profiles, *Earth Planet. Sci. Lett.*, *317–318*, 27–43.
- Kiefer, B., L. Stixrude, and R. M. Wentzcovitch (2002), Elasticity of (Mg, Fe)SiO₃-perovskite at high pressures, *Geophys. Res. Lett.*, *29*(11), 1539, doi:10.1029/2002GL014683.

- Klemens, P. G., G. K. White, and R. J. Tainsh (1962), Scattering of lattice waves by point defects, *Philos. Mag.*, *7*(80), 1323–1335, doi:10.1080/14786436208213166.
- Konôpková, Z., R. S. McWilliams, N. Gómez-Pérez, and A. F. Goncharov (2016), Direct measurement of thermal conductivity in solid iron at planetary core conditions, *Nature*, *534*(7605), 99–101, doi:10.1038/nature18009.
- Lay, T., J. Hernlund, and B. A. Buffett (2008), Core–mantle boundary heat flow, *Nat. Geosci.*, *1*(1), 25–32, doi:10.1038/ngeo.2007.44.
- Lin, J.-F., et al. (2008), Intermediate-spin ferrous iron in lowermost mantle post-perovskite and perovskite, *Nat. Geosci.*, *1*(10), 688–691, doi:10.1038/ngeo310.
- Lin, J.-F., S. Speziale, Z. Mao, H. Marquardt, and G. Science (2013), Effects of the electronic spin transitions of iron in lower-mantle minerals: Implications for deep-mantle geophysics and geochemistry, *Rev. Geophys.*, *51*, 244–275, doi:10.1002/rog.20010.
- Lin, J.-F., Z. Mao, J. Yang, J. Liu, Y. Xiao, P. Chow, and T. Okuchi (2016), High-spin Fe²⁺ and Fe³⁺ in single-crystal aluminous bridgmanite in the lower mantle, *Geophys. Res. Lett.*, *43*, doi:10.1002/2016GL069836.
- Manthilake, G. M., N. de Koker, D. J. Frost, and C. A. McCammon (2011), Lattice thermal conductivity of lower mantle minerals and heat flux from Earth's core, *Proc. Natl. Acad. Sci. U.S.A.*, *108*(44), 17,901–17,904, doi:10.1073/pnas.1110594108.
- Mao, H. K., P. M. Bell, J. W. Shaner, and D. J. Steinberg (1978), Specific volume measurements of Cu, Mo, Pd, and Ag and calibration of the ruby R1 fluorescence pressure gauge from 0.06 to 1 mbar, *J. Appl. Phys.*, *49*(6), 3276–3283, doi:10.1063/1.325277.
- Mao, Z., et al. (2017), Equation of state and hyperfine parameters of high-spin bridgmanite in the Earth's lower mantle by synchrotron X-ray diffraction and Mossbauer spectroscopy, *Am. Mineral.*, *102*, 357–368.
- McCammon, C., I. Kantor, O. Narygina, J. Rouquette, U. Ponkratz, I. Sergueev, M. Mezouar, V. Prakapenka, and L. Dubrovinsky (2008), Stable intermediate-spin ferrous iron in lower-mantle perovskite, *Nat. Geosci.*, *1*(10), 684–687, doi:10.1038/ngeo309.
- Mosca, I., L. Cobden, A. Deuss, J. Ritsema, and J. Trampert (2012), Seismic and mineralogical structures of the lower mantle from probabilistic tomography, *J. Geophys. Res.*, *117*, B06304, doi:10.1029/2011JB008851.
- Murakami, M., K. Hirose, K. Kawamura, N. Sata, and Y. Ohishi (2004), Post-perovskite phase transition in MgSiO₃, *Science*, *304*(5672), 855–858, doi:10.1126/science.1095932.
- Ohta, K., T. Yagi, N. Taketoshi, K. Hirose, T. Komabayashi, T. Baba, Y. Ohishi, and J. Hernlund (2012), Lattice thermal conductivity of MgSiO₃ perovskite and post-perovskite at the core–mantle boundary, *Earth Planet. Sci. Lett.*, *349–350*, 109–115, doi:10.1016/j.epsl.2012.06.043.
- Okuchi, T., N. Purevjav, N. Tomioka, J.-F. Lin, T. Kuribayashi, L. Schoneveld, H. Hwang, N. Sakamoto, N. Kawasaki, and H. Yurimoto (2015), Synthesis of large and homogeneous single crystals of water-bearing minerals by slow cooling at deep-mantle pressures, *Am. Mineral.*, *100*, 1483–1492.
- Olson, P., and U. R. Christensen (2002), The time-averaged magnetic field in numerical dynamos with non-uniform boundary heat flow, *Geophys. J. Int.*, *151*(3), 809–823, doi:10.1046/j.1365-246X.2002.01818.x.
- Osako, M., and E. Ito (1991), Thermal diffusivity of MgSiO₃ perovskite, *Geophys. Res. Lett.*, *18*(2), 239–242, doi:10.1029/91GL00212.
- Potapkin, V., et al. (2013), Effect of iron oxidation state on the electrical conductivity of the Earth's lower mantle, *Nat. Commun.*, *4*, 1427, doi:10.1038/ncomms2436.
- Rudolph, M. L., V. Leki, and C. Lithgow-bertelloni (2015), Viscosity jump in Earth's mid-mantle, *Science*, *350*(6266), 1349–1352, doi:10.1126/science.1251929.
- Schmidt, A., M. Chiesa, X. Chen, and G. Chen (2008), An optical pump-probe technique for measuring the thermal conductivity of liquids, *Rev. Sci. Instrum.*, *79*, 64902, doi:10.1063/1.2937458.
- Shukla, G., Z. Wu, H. Hsu, A. Floris, M. Cococcioni, and R. M. Wentzcovitch (2015), Thermoelasticity of Fe²⁺-bearing bridgmanite, *Geophys. Res. Lett.*, *42*, 1741–1749, doi:10.1002/2014GL062888.
- Stackhouse, S., L. Stixrude, and B. B. Karki (2015), First-principles calculations of the lattice thermal conductivity of the lower mantle, *Earth Planet. Sci. Lett.*, *427*, 11–17, doi:10.1016/j.epsl.2015.06.050.
- Tackley, P. J. (2012), Dynamics and evolution of the deep mantle resulting from thermal, chemical, phase and melting effects, *Earth Sci. Rev.*, *110*(1–4), 1–25, doi:10.1016/j.earscirev.2011.10.001.
- Tang, X., M. C. Ntam, J. Dong, E. S. Rainey, and A. Kavner (2014), The thermal conductivity of Earth's lower mantle, *Geophys. Res. Lett.*, *41*, 2746–2752, doi:10.1002/2013GL058954.
- Trampert, J., F. Deschamps, J. S. Resovsky, and D. A. Yuen (2004), Probabilistic tomography maps chemical probabilistic tomography maps chemical heterogeneities throughout the lower mantle, *Science*, *306*, 853–856, doi:10.1126/science.1101996.
- Tsuchiya, J., T. Tsuchiya, and R. M. Wentzcovitch (2005), Vibrational and thermodynamic properties of MgSiO₃ postperovskite, *J. Geophys. Res.*, *110*, B02204, doi:10.1029/2004JB003409.
- Xu, Y., T. J. Shankland, S. Linhardt, D. C. Rubie, F. Langenhorst, and K. Klasinski (2004), Thermal diffusivity and conductivity of olivine, wadsleyite and ringwoodite to 20 GPa and 1373 K, *Phys. Earth Planet. Inter.*, *143*, 321–336, doi:10.1016/j.pepi.2004.03.005.
- Zheng, X., D. G. Cahill, P. Krasnochtchekov, R. S. Averback, and J. C. Zhao (2007), High-throughput thermal conductivity measurements of nickel solid solutions and the applicability of the Wiedemann-Franz law, *Acta Mater.*, *55*(15), 5177–5185, doi:10.1016/j.actamat.2007.05.037.